On the implication of mobile hydrogen content on the surface reactivity of an austenitic stainless steel

Malo Duportal, Abdelali Oudriss, C. Savall, Alexis Renaud, Christine Labrugère-Sarroste, Xavier Feaugas

On the implication of mobile hydrogen content on the surface reactivity of an austenitic stainless steel

Duportal Malo[a], Oudriss Abdelali[a], Savall Catherine[a], Renaud Alexis[a], Labrugère-Sarroste Christine[b] and Feaugas Xavier[a]

Corresponding authors: malo.duportal@univ-lr.fr; catherine.savall@univ-lr.fr

[a]*La Rochelle University, LaSIE UMR CNRS 7356, Av. Michel Crépeau, 17042 La Rochelle, France*

[b]*PLACAMAT UMS 3626, CNRS, Université de Bordeaux, 87 avenue du Dr Albert Schweitzer, 33608 Pessac Cedex, France*

Keywords: *Hydrogen absorption, dissolution kinetics, hydrogen oxidation, passive films properties, AISI 316L*

Highlights

H-absorption induces an increase of the surface activity.

Dissolution rate is widely affected by H-absorption while the passive layer growth rate and chemical composition are not strongly affected.

The increase of surface activity is mainly reversible with H-desorption highlighting the role of mobile H.

The Point Defect Model suggests an increase of the vacancies mobility due to H-absorption

Abstract

The Influence of hydrogen on the corrosion behavior of an AISI 316L austenitic stainless steel in borate buffer solution is studied after a cathodic pre-charging step. A high amount of hydrogen is absorbed and forms a concentration gradient from the surface to the bulk with a

path length of about 80 µm. The surface reactivity in the passive regime after the cathodic charging and during the hydrogen desorption is investigated with a large set of electrochemical and physico-chemical technics: electrochemical polarization, EIS, Mott-Schottky analysis and XPS. This approach allows to demonstrate that surface reactivity increases drastically with hydrogen absorption. This effect is mostly due to mobile hydrogen and is mainly reversible with its desorption. Hydrogen absorption and desorption have a small impact on the passive layer composition and thickness. However, the hydrogen induces an increase in the dissolution rate, which is discussed based on the Point Defect Model. Present results suggest that the impact of hydrogen on the surface reactivity is a consequence of a strong increase in the mobility of anionic vacancy and/or hydrogen oxidation.

1. Introduction

Today, the hydrogen production is mainly issued from gas and oil industry, but some new green technologies based on water reduction regularly emerge. Then hydrogen production can be managed applying an electrical current between two electrodes leading to the reduction of water [1]. This reaction might also occur on a metal surface in aqueous environment, especially when galvanic coupling is used to protect a metal piece. All of these situations, as well as the use of hydrogen gas as a vector of energy, or as a corrosion accelerator in some medical applications, can lead to hydrogen absorption through the steel. In some circumstances, this absorption can promote a mechanical degradation, better known as hydrogen embrittlement [2]. Despite Hydrogen Embrittlement (HE) has been widely studied during these last years, the consequence of the absorption of hydrogen on corrosion behaviors has only been the topic of very few publications. In fact, an inherent modification of materials properties, especially surface properties due to hydrogen ingress, could interfere with the corrosion process [3–5]. As the hydrogen affects the metal bonds [6], we can expect an

alteration of dissolution and passivation mechanisms [7]. Hence, it is complex to predict the impact of hydrogen on the sustainability of the materials since the passive layer stability depends on a competition between these two phenomena. In this context, this work aims to make a deep investigation of the role of the local hydrogen concentration on the properties of passive layers formed in a borate buffer solution on an annealed austenitic stainless steel AISI 316L. Hydrogen has a high solubility in face centered cubic (fcc) steels and a low diffusion coefficient allowing to reach an important hydrogen gradient [8]. In addition, AISI 316L presents a stable austenitic phase and few metallurgical defects which could act as hydrogen traps [9]. Absorbed hydrogen is commonly described using a diffusion activation energy model. A low energy is attributed to diffusible hydrogen while a high energy corresponds to trapped hydrogen. A high energy is frequently associated to the presence of metallurgical defects such as dislocations, vacancies, grains boundaries, elastic fields [10]. Finally, borate buffer solution allows to form a stable oxide layer with low dissolution kinetics (thus facilitating the study of an oxide layer) [4, 11–20].

Based on Electrochemical Impedance Spectroscopy (EIS) and anodic polarization experiments on 316LN stainless steel, Ningshen *et al.* observed that the hydrogen absorption leads to a decrease in the passive film stability and in the pitting corrosion resistance [3, 4]. Due to the difficulties in quantifying hydrogen content, few studies propose an analysis of the absorbed hydrogen concentration in an austenitic stainless steel combined with the characterization of the electrochemical behavior of the material after hydrogen absorption [14, 21–23]. In particular, Yang *et al.* [14] observed a decrease in the passive layer thickness and a modification of its chemical composition by XPS for a AISI 310 stainless steel previously charged with 8.0 ± 0.3 wppm of hydrogen. In their work, Mott-Schottky tests revealed that hydrogen can cause an inversion of the conductivity type of the oxide film from p-type to n-

type. Finally, they suggested that hydrogen absorption reduced the stability of the passive layer and increased its susceptibility to pitting.

A previous study attests the formation of an important hydrogen concentration gradient in 316L stainless steel after 72 hours of cathodic charging in 0.1M NaOH + NH_4SCN ($3g.L^{-1}$) at $-100\ mA.cm^{-2}$ and 50°C [24]. To our best knowledge, a correlation between the local hydrogen concentration and the electrochemical behavior of austenitic stainless steel has never been reported in the literature. This relation seems obvious since electrochemical processes, as passivation and dissolution, are surface phenomena. Moreover, only few research works [23, 25] focus on the hydrogen desorption which will allows here to distinguish the reversible effects attributed to diffusible hydrogen from the irreversible effects attributed to trapped hydrogen. A first study, conducted by Yashiro *et al.* [25], proposed a partially reversible effect of hydrogen on the pitting potential throughout the desorption. Unfortunately, this observation has not been correlated to hydrogen concentration and needs to be investigated thoroughly and clarified with complementary electrochemical analysis.

The general purpose of this work is to determine the role of the hydrogen concentration and mobility on the electrochemical behavior of an austenitic stainless steel, especially by focusing on the passive layer stability and the surface kinetics in the passive range. To this end, the metallurgical characterization of the studied material was firstly performed at different scales (SEM, EBSD, AFM, TEM…) and will be not extensively described there. Secondly, samples were electrochemically charged in a sodium hydroxide solution with ammonium thiocyanate. Then, the total hydrogen concentration was quantified by hot extraction, and the concentration gradient under the surface was evaluated. Stationary and non-stationary electrochemical tests were conducted to evaluate the influence of hydrogen charging and hydrogen desorption on the behavior of the passive layer. For that purpose, the anodic processes were studied in a borate buffer solution. The formation of the passive layer,

before and after hydrogen charging, was investigated by anodic polarization and chrono-amperometry. Electrochemical Impedance Spectroscopy (EIS), Mott-Schottky and X-ray Photoelectron Spectrometry (XPS) tests were conducted to characterize the passive layer properties.

2. Experimental

2.1 Material and hydrogen charging protocol

The material employed in the present study was an AISI 316L austenitic stainless steel. The chemical composition of this steel is shown in Table 1. Grain size, crystallographic texture, grain-boundaries character, and dislocations density were previously investigated using scanning electron microscopy coupled to Electronic Back Scattering Diffraction (SEM-EBSD) and Transmission Electronic Microscopy (TEM). According to these characterizations, the average grain diameter was evaluated to be around 53±19 µm, no preferential grain orientation is detected with 45% of random grain boundaries [9, 24, 26].

Table 1: Average composition of the studied AISI 316L austenitic stainless steel [26]**.**

Fe	Cr	Ni	Mo	Si	N	C	Mn	Co	Cu
Balance	**17.54**	**12.46**	**2.48**	**0.44**	**0.08**	**0.03**	**1.88**	**0.15**	**0.18**

Specimens were embedded in an epoxy resin and the working area was 1 cm² for the electrochemical tests. The working surface was subsequently grinded from 1000 grit to 4000 grit emery paper, resulting in a surface roughness (RMS) of 16 nm estimated by Atomic Force Microscopy (AFM). Grinded samples were then cleaned using distilled water and ethanol. Using TEM, the surface density of dislocations was estimated at around 5.10^{11} m^{-2}. This value is close to the density of dislocations estimated in the bulk in a previous study [9, 26].

The hydrogen charging solution was composed of NaOH 0.1 mol.L^{-1} and NH_4SCN 3 g.L^{-1}. Ammonium thiocyanate was used to promote hydrogen absorption [27]. The reference electrode was a sulfate saturated reference electrode (ESS) and the counter electrode a platinum grid. Hydrogen charging was performed using electrochemical cathodic method by applying a current density of -100 mA.cm^{-2} in the solution described above, at 50°C. For all electrochemical tests as well as for XPS analysis, samples were electrochemically charged for 72h. After hydrogen charging, samples with a thickness of 500 µm were briefly grinded with a 4000 grit emery paper, cleaned with acetone, dried with air and then were characterized to determine the total hydrogen concentration by Hot extraction (EMGA 621 H-Analyzer from Horiba) as a function of desorption time in air at room temperature.

2.2 Electrochemical measurements

A borate buffer solution (12.2 g.L^{-1} of $B(OH)_3$ and 19.0 g.L^{-1} of $Na_2B_4O_7$, pH 8.4) was used in this work to study the passive layer behavior. All electrochemical tests were carried out at 25°C in about 400 mL of the deaerated (argon) solution. A three-electrode cell was employed with Pt as a counter electrode and a saturated calomel electrode (SCE) as reference electrode. In this study, all potential values are relative to the SCE.

Electrochemical measurements including potentiodynamic polarization curves, potentiostatic current curves, Mott-Schottky and Electrochemical Impedance Spectroscopy (EIS) were performed on circular samples of 1 cm² and were reproduced a least three time. The analyzed batch includes uncharged, 72h hydrogen charged and different desorption time (24h, 48h, 72h, 168h) specimens. The hydrogen charging time (72h) was defined to maximize the apparent solubility in the charging conditions described in a previous paper [24]. The transfer time from the hydrogen charging cell to the electrochemical cell was of about 5 minutes (during which samples are mechanically grinded with 4000 SiC in order to remove the residual oxide layer).

Electrochemical measurements were performed through a VSP potentiostat from Bio-logic® . Potentiodynamic polarization curves were recorded with a potential scan rate of 0.25 $mV.s^{-1}$. A pre-polarization with a current density of -500 $\mu A.cm^{-2}$ was applied for 15 minutes, as suggested in protocols from other studies [15, 17, 18], and then a potentiostatic polarization step was performed during 1h at -0.1 V_{ECS} (passive range).

EIS and Mott-Schottky measurements were done after two pre-treatment steps consisting in a cathodic polarization (as previously describes) and an anodic polarization (1 hour at -0.1 V_{ECS}) to form a stable passive layer. Then, EIS measurements were carried out at 0.1 V_{ECS} from 100 kHz to 10 mHz with 10 points per decades and a sinus amplitude of 10 mV. Mott-Schottky analyses were achieved at 1 kHz from -300 mV_{ECS} to 600 mV_{ECS}.

2.3 X-ray photoelectron spectrometry (XPS)

X-ray photoelectron spectrometry was carried out to get information on the passive layer composition and thickness before and after hydrogen absorption. For that purpose, a stable passive layer was formed by maintaining a potentiostatic current for 1 hour at -0.1 V_{SCE} just after a cathodic polarization at a current density of -500 $\mu A.cm^{-2}$ for 15 minutes. Samples were then stored in an argon atmosphere at atmospheric pressure during the transfer to XPS equipment (Thermo Scientific K-Alpha). All spectra were acquired using a monochromatized Al–Kα radiation (1486.6 eV), yielding a focused X-ray spot with 200 µm diameter with a normal emission angle, analyzer pass energy fixed at 40 eV for high resolution spectra. All specimens were sputtered with Ar^+ ions. The abrasion rate was calibrated using a mechanical profilometer after an abrasion time of 5000s and was estimated to be around 0.2 $nm.s^{-1}$ (considering that abrasion rate is equivalent for the bulk and for the oxidized surface of the sample). The erosion sequence was 1s eight times then 10s to obtain the oxide film depth profile and therefore the thickness of the passive layer. High resolution spectra (i.e. C1s, O1s, Fe2p, Cr2p, Ni2p, Mo3d) were quantified (Scofield sensitivity factors applied) and/or fitted

using the XPSPEAK 4.1 software. The main element of the spectra were fitted as follow: (i) O1s with 3 components, oxide (~530.3 eV), hydroxide (~531.8 eV), H_2O or O-C contaminations (~533.2 eV) respectively, (ii) $Fe2p_{3/2}$ part of the Fe2p spectra with 5 components, the first three attributed to metallic iron (~707.0 eV), Fe^{2+} (~709.1 eV), Fe^{3+} (~711.5 eV) respectively [12, 28–31], (iii) $Cr2p_{3/2}$ part of the Cr2p spectra with 3 components corresponding to metallic chromium (~574.1 eV), Cr^{3+} oxide (~576.5 eV) and Cr^{3+} hydroxide (~577.6 eV) [12, 28, 29, 31–33], (iv) $Ni2p_{3/2}$ part of the Ni2p spectra with 3 components attributed to metallic nickel (~852.9 eV) and its satellite (~859.0 eV), and one oxidized Ni form (~855.7 eV) [12, 28], and finally (v) $Mo3d_{5/2}$ part of the Mo3d spectra with 3 components assigned to metallic form (~227.8 eV), Mo^{4+} (~229.1 eV) and Mo^{6+} (~232.5 eV) [12, 30–32].

3. Experimental results

3.1 Hydrogen concentration

First, the AISI 316L samples were cathodically charged during 72h and hydrogen ingress was characterized by hot extraction analysis immediately after 72h of charging and also after different desorption times (see reference [24] for more details). The total hydrogen concentration is of 80±17 wppm (on a sample with a thickness of 500 µm). These results are in line with another study performed under similar conditions [34]. Figure 1-a presents the evolution of the local H concentration with respect to the desorption time at ambient temperature and pressure (300 K, 1 atm) following the method presented in a previous paper [24]. In Figure 1-b, reproduced from this previous work [24], it was shown on GD-OES profiles (confirmed by SKPFM) that under the same H-charging conditions, the hydrogen was localized within a layer of 76 µm beneath the surface. This allowed to estimate the H mean

concentration in this layer, which will be referred to as $[H]_{local}$ in the following and which is about 520 wppm after 72 hours of cathodic charging. This approach also allowed to estimate an apparent hydrogen diffusion coefficient of around 2.10^{-15} $m^2.s^{-1}$ thanks to Fick's laws. In these conditions, a rapid desorption of hydrogen is observed during the first hours and reaches a plateau of local concentration at around 105±46 wppm after 48 hours of desorption.

Figure 1: (a) Evolution of local hydrogen concentration (wppm) with desorption time (b) profil of hydrogen distribution estimated by GD-OES after 72h of cathodic charging in NaOH 0.1M + NH4SCN 3g/L at 50°C and -100 mA/cm² [24]**.**

In order to follow the influence of the desorption time on the electrochemical behavior, different desorption times were selected for the following of the paper, namely 24h, 48h, 72h and 168h.

3.2 Dynamic Polarization curves

Dynamic polarization curves are presented in Figure 2-a for different desorption times. For the uncharged specimen, the corrosion potential is around -638 mV_{SCE}. A very weak peak (1.8 $\mu A.cm^{-2}$) is observed followed by a quasi-plateau with a passive current density of around 1.1 $\mu A.cm^{-2}$. The increase in the current density after 0.9 V_{SCE} is due to the oxidation of water. This behavior is in good agreement with the behavior of austenitic stainless steels described in the literature [12, 14, 16, 19]. Two small peaks are observed on the passive plateau. Several studies conducted in a similar environment assume that the first peak, around -0.2 V_{SCE}, probably corresponds to the oxidation of some species of the pre-passive film [11, 12, 35, 36] and the second peak, at 0.6 V_{SCE}, probably corresponds to a deficit of stability of chromium at such potential [11, 12, 14, 36]. A 72h cathodic charging induces a decrease in the corrosion

potential, an increase in the critical current and passive current densities, while the cathodic branch does not seem to be modified.

Finally, as the desorption of hydrogen progresses, the current densities progressively decrease and the corrosion potential tends also to shift towards the values of uncharged samples. Different kinetics parameters obtained from the polarization curves are presented in Table 2, which also gives the local H concentration $[H]_{local}$, as previously defined, for the different conditions (desorption time). J_{crit} and E_{crit} refer to the small peak observed before the passive region. All these parameters suggest that H ingress increases the anodic activity and that the observed effects are partially reversible after hydrogen desorption. In the following, we will focus on the behavior in the passive region, which seems particularly sensitive to the $[H]_{local}$ concentration.

Figure 2: Anodic polarization curves at 0.25 mV.s^{-1} in borate buffer (pH 8.4) of a AISI 316L stainless steel before, after cathodic charging, and for different desorption times.

Table 2: Data from dynamic polarization curves.

Samples	**$[H]_{local}$ (wppm)**	**E_{corr} (mV_{SCE})**	**J_{crit} ($\mu A.cm^{-2}$)/ E_{crit} (mV_{SCE})**	**J_{pass} ($\mu A.cm^{-2}$ at -0.1 V_{SCE})**
Uncharged	0	-638	1.8 (-413)	1.1
72h Charged	533	-720	/	4.0
24h Desorbed	192	-723	4.5 (-440)	2.4
48h Desorbed	119	-734	2.9 (-414)	2.0
72h Desorbed	114	-708	2.3 (-439)	1.8
168h Desorbed	106	-675	/	1.9

3.3 Potentiostatic current

Figure 3-a presents potentiostatic anodic current curves obtained at the applied potential of -0.1 V_{SCE} for different conditions in order to study the kinetics of the formation and the stability of the passive film after a cathodic treatment at -500 µA.cm^{-2}. For the uncharged specimen, a fast decay of the current density occurs at the beginning, which is due to the formation of the passive film. Then, the current density reaches a steady state (J_{SS}) at 0.176 ± 0.002 µA.cm^{-2}. This current density is obtained by averaging on the last 100 seconds and is presented in Table 3 for the different specimens and conditions. After the cathodic charging, the general shape of the curve is similar, but the stationary current density is drastically increased and reaches 2.682 ± 0.007 µA.cm^{-2}. The stationary current density decreases progressively with desorption time and almost reaches the value of uncharged samples. Several papers have studied the repassivation kinetics of stainless steels [16, 37–39]. After a fast step of initial nucleation and development of a first atomic oxide layer [16, 38] (around 370 ms for an AISI 316L stainless steel in borate buffer solution from *Xu et al.* [16]), the passive layer growth follows the high electric field ion conduction model [16, 38, 39]. This model assumes the formation of a high electric field (around 10^6 V.cm^{-1} [16, 39]) across the passive layer leading to the migration of cations through the film to the surface and inducing the passive layer growth. Assuming that no significant dissolution happens during film formation [16, 37–39], the passive current can be described using the empirical relation used by many authors to estimate the oxide growth kinetics on stainless steel [40–43] and other alloys [44, 45]:

$$\log J(t) = C - \alpha . \log t \quad (1)$$

with C a constant, $J(t)$ and t the current density and time, and α the slope of the initial stage of log $J(t)$ vs log t plot. As polarization time increases, the passive film thickens and the

electric field decreases, so the contribution of dissolution phenomena to the current is no longer negligible and the current density deviates from this model.

Figure 3: (a) Anodic polarization curves at -0.1 V_{SCE} in borate buffer (pH 8.4) of a AISI 316L stainless steel before, after cathodic charging, and for different desorption time. (b) Determination of C and α parameters by linear regressions.

Figure 3b presents ln J versus ln t curves between 370 ms [16] and 2 s for uncharged, 72h charged and desorbed samples. The chosen time range was in accordance with the work of Xu on a 316L stainless steel in borate buffer solutions [16]. Linear regressions provide the values of the C and α constants which are reported in Table 3. The values of the coefficient α are nearly 1, which is in good agreement with the data in the literature [16, 44, 46]. A slight decrease in the coefficient α can be highlighted after hydrogen ingress (from 0.94 to 0.85). This decrease in the parameter value was explained by some authors by a reduction of the protective nature of the passive layer [44] which corresponds to a slight decrease in the film growth kinetics. Then Table 3 shows that a gradual shift of this coefficient to the initial value is observed throughout desorption.

Assuming that the growth kinetics of the passive film follows relation (1) and using the parameters deduced from Table 3, the corrected anodic density of current (J_{ca}), corresponding to all "anodic reactions" except film growth, was calculated by the relation:

$$J_{ca}(t) = J_{exp}(t) - J_{growth}(t) \quad (2)$$

With $J_{exp}(t)$ the experimental current density and $J_{growth}(t)$ the growth current density. These current densities are plotted *versus* time for uncharged and 72h charged samples in Figure 4-a and b respectively.

Figure 4: Plots of J_{exp} (experimental current density), J_{growth} (oxide growth current density) and J_{ca} (corrected anodic density of current) for AISI 316L stainless steel (a) Uncharged (b) 72h Charged.

Figure 4-a suggests that the experimental current density is widely dictated by the oxide growth for the uncharged sample. After 72h of cathodic charging, J_{ca} markedly increases, and the current density is governed by other anodic processes such as dissolution of the passive film or other anodic processes. Table 3 presents the passive current ($J_{SSgrowth}$) and the corrected anodic current (J_{SSca}) at the steady state (obtained by averaging on the last 100 seconds) compared with the experimental value (J_{SSexp}). This table shows that, as desorption time increases, J_{SSca} progressively decreases. This confirms that the effect of hydrogen is partially reversible with desorption time. It can be deduced from Table 3, that the oxide growth current seems not to be much affected by cathodic charging or hydrogen desorption. In contrast, it seems that the other anodic processes are mostly impacted by hydrogen charging and desorption.

Table 3: Data from static polarization curves.

Samples	$[H]_{local}$ (wppm)	J_{SSexp} ($\mu A.cm^{-2}$)	α	C	$J_{SSgrowth}$ ($\mu A.cm^{-2}$)	J_{SSca} ($\mu A.cm^{-2}$)
Uncharged	0	0.176 ± 0.002	0.938	-8.198	0.129 ± 0.001	0.047 ± 0.001
72h Charged	533	2.682 ± 0.007	0.852	-8.052	0.301 ± 0.002	2.381 ± 0.005
24h Desorbed	192	0.658 ± 0.002	0.903	-8.202	0.171 ± 0.001	0.487 ± 0.001
48h Desorbed	119	0.437 ± 0.002	0.874	-8.290	0.198 ± 0.001	0.239 ± 0.001
72h Desorbed	114	0.381 ± 0.002	0.874	-8.235	0.209 ± 0.002	0.172 ± 0.001
168h Desorbed	106	0.212 ± 0.001	0.925	-8.403	0.117 ± 0.001	0.095 ± 0.001

3.4 Electrochemical Impedance Spectroscopy

In order to deeply investigate the passive film properties formed on AISI 316L stainless steel, EIS measurements were conducted at an applied potential of -0.1 V_{SCE} after 15 minutes of cathodic treatment at -500 µA.cm^{-2} and 1h of film formation at -0.1 V_{SCE}. The EIS results are presented in the form of Bode and Nyquist plots in Figure 5-a (modulus from bode plots), b (phase from bode plots) and c (Nyquist plots). Results suggest, as seen on Bode diagrams, that hydrogen charging mainly affects the low frequencies range rather than the high frequencies one. The Nyquist representation suggests that the uncharged sample presents a quasi-blocking behavior, which does not allow the formation of a capacitive semicircle in the investigated frequency range, in line with the presence of a homogeneous and continuous passive layer [47, 48]. Impedance modulus drastically decreases after hydrogen charging, suggesting that this effect seems to be partially reversible with hydrogen desorption.

Figure 5: EIS pattern and corresponding fitting (solid lines) of AISI 316L stainless steel at -0.1V_{SCE} in borate buffer (a) Modulus and (b) Phase from Bode plots (c) Nyquist plots for uncharged, 72h charged and different desorption times.

The simulation of passive layers EIS spectra, represented with solid lines in Figure 5, has been widely discussed in the literature [29, 47–58]. One electrical model emerges in similar environments [54–58] and is presented in Figure 6. This model uses two time constants as suggested by profiles of the phase diagrams from Bode plots.

Figure 6: Used electrical model to fit EIS in Borate Buffer solution.

This model allows to fit impedance data obtained in a borate buffer solution because the passive layer is assumed to be really covering without any defects (no pitting happens on anodic polarization curves (*cf.* Figure 2)). Here, R_s is the electrolyte resistance, C_1 and R_1 are linked with electrical double layer and the charge transfer resistance whereas Q_2 and R_2 are associated with non-ideal capacitive and resistive behavior of the oxide film [53, 56–59]. A constant phase element (CPE) was used for the oxide layer because the measured capacitances are frequently not ideal (attributed for example to variations in the thickness or chemical composition). CPE is defined by:

$$Z_{CPE} = \frac{1}{(j\omega)^{\alpha} Q} \quad (3)$$

with Q ($F.cm^{-2}.s^{(\alpha-1)}$) representing the CPE intrinsically linked to α which represents the deviation from a purely capacitive behavior (if α=0 the CPE is purely resistive, if α=1 the CPE is a pure capacitance), ω is the pulsation (=2πf).

Fitting was managed thanks to *Simad*® software developed at *Laboratoire Interfaces et Systèmes Electrochimiques (LISE Lab CNRS UMR 8235)*. The fitting results are displayed as solid lines in Figure 5 and obtained values are presented in Table 4:

Table 4: EIS results obtained by fitting with electrical model for a AISI 316L uncharged 72h charged and desorbed.

Samples	$[H]_{local}$ (wppm)	R_s ($Ohm.cm^2$)	C_1 (10^{-6} $F.cm^{-2}$)	R_1 (10^4 $Ohm.cm^2$)	Q_2 (10^{-6} $F.cm^{-2}.s^{\alpha-1}$)	α_2	R_2 (10^4 $Ohm.cm^2$)	C_{CPE} (10^{-6} $F.cm^{-2}$)
Uncharged	0	41.5	195	1.22	33.0	0.926	151	6.96
72h Charged	533	25.7	102	1.23	59.5	0.876	16.4	4.43
24h Desorbed	192	24.0	180	1.80	37.2	0.910	59.5	5.58

48h Desorbed	119	38.5	167	1.90	34.7	0.921	96.9	6.62
72h Desorbed	114	25.8	190	1.39	35.5	0.919	97.0	6.54
168h Desorbed	106	48.3	195	2.11	35.0	0.922	130	6.84

We first focus on the capacity of the double layer. This capacity slightly decreases after hydrogen charging and increases upon desorption, but the variations are relatively weak. Obtained values, ranging between 100 and 200 $\mu F.cm^{-2}$, are conform with the literature for a double layer capacity on similar systems [59, 60].

Then, we can focus on the evolution of the resistances in a borate buffer solution. The resistance R_1, attributed to charge transfer, does not show significant variations after hydrogen ingress or hydrogen desorption. Furthermore, the oxide film resistance (R_2) shows a strong decrease, which expresses a poorer protection against corrosion after hydrogen ingress. Then, this resistance increases with desorption time. The degradation of this protection can be due to many factors as a variation in the oxide composition or the formation of defects that cannot be precisely determined by EIS. The difference between resistances R_1 and R_2 of about two orders of magnitude consolidates the physical meaning of the equivalent electrical circuit and is in good agreement with the literature [59]. Impedance suggests that charge transfer resistance is not significantly affected by cathodic charging unlike the film resistance. This last resistance, being the highest so the limiting factor, allows to explain the increases in the density of current at the steady state after cathodic charging previously observed.

Concerning the constant phase element (Q, α), attributed to the passive film, Table 4 shows that the corrector exponent (α) is close to 1, indicating a mainly capacitive behavior. This

exponent cannot be analyzed alone and has to be linked with the coefficient Q [61]. The constant phase element (CPE) model is a mathematical tool to describe a non-ideal capacitive behavior (as a capacitive gradient) but it gives no indication on physical processes [48]. Hirshorn *et al.* [49] showed that a normal distribution has to be considered for an oxide passive layer. Therefore, the power law distribution allows to calculate the capacitance (C_{CPE}) using the following equations by Hirschorn *et al.* [48, 62] for a blocking behavior:

$$C_{CPE} = Q.(\rho_{\delta}.\varepsilon.\varepsilon_0)^{1-\alpha}.g \quad (4)$$

where C_{CPE} is the calculated capacitance using CPE fitted data, Q and α are the parameters of the CPE, ε and ε_0 are respectively the vacuum permittivity (8.85 x 10^{-14} F.cm^{-1}) and the relative permittivity of the oxide assumed to be constant and has a value of 15.6 [17, 29, 48, 51]. ρ_{δ} is the resistivity of the interface and assigned to a value of 500 Ω.cm [46, 47, 51] (consistent with the value of 450 Ω.cm obtained by Hirschorn *et al.* [48] for a stainless steel). g is a function that was numerically evaluated and could be expressed as [48, 62]:

$$g = 1 + 2.88(1-\alpha)^{2.375} \quad (5)$$

Obtained capacities from equation (4) are given in Table 4 and are consistent with the literature for a passive layer capacity in near neutral environment [47, 48]. They do not show a marked evolution after H charging and desorption.

Assuming a capacitance proportional with the film thickness, the passive layer thickness (d_{film}) can be approximated from the calculated capacitance related to the local dielectric constant (ε_0) [48, 49]:

$$C = \frac{\varepsilon.\varepsilon_0}{d_{film}} \quad (6)$$

The thickness of the passive film was evaluated by using this relation. The obtained value is about 2 nm for the uncharged sample, congruent with many works from the literature that

determine oxide layer thicknesses using different methods (EIS, XPS, chrono-amperometry, TEM, AES) on stainless steel in borate buffer [16, 17, 19, 20, 47]. According to the slight variations of the C_{CPE} parameter in Table 4, it can be deduced that the thickness of the passive film does not seem to markedly vary upon charging and desorption.

The degradation of the protection against corrosion can be due to many factors as variation in oxide composition or defects formation which cannot be precisely determined by EIS. That is why X-ray photoelectron spectrometry (XPS) is presented in the next part.

3.5 X-ray photoelectron spectrometry (XPS)

XPS tests were conducted after 1 hour of passivation at -0.1 V_{ECS} in a borate buffer environment. XPS high-resolution spectra O1s, Fe2p, Cr2p and Ni2p, obtained after 0s and 4s sputtering, before and after hydrogen ingress, are given in Figure 7. The Fe2p, Cr2p and Ni2p spectra are normalized compare to the local highest peak allowing a better comparison between the different sputtering times. On the contrary, O1s spectrum corresponds to high-resolution spectra, allowing to determine the decrease in oxide content. High-resolution Mo3d spectra are not shown as metal base concentration is low.

Figure 7: High-resolution XPS spectra of uncharged and 72h charged samples passivated 1h at -0.1V_{ECS} in borate buffer, after 0s and 4s sputtering (a) O1s (b) $Fe2p_{3/2}$ (c) $Cr2p_{3/2}$ and (d) $Ni2p_{3/2}$.

Figure 7- a, b, c attests a strong decrease in the oxide contributions after 4 seconds of ion sputtering. Figure 7- d shows that nickel oxides are roughly lacking in the passive layer in accordance with bibliographic data on similar systems [63, 64]. It can be noticed that, even without any sputtering, both Fe and Cr metallic components are observed due to the contribution of the underlying metal. Fitted $Fe2p_{3/2}$, $Cr2p_{3/2}$, $Ni2p_{3/2}$ and $Mo3d_{5/2}$ spectra for

each abrasion time allow to reconstruct the depth concentration profile of each chemical environment for the passive layer and underlying metal (Figure 8). Note that these depth profiles are given without subtracting the metal components from underlying layers. The estimated depth is given under the consideration that the previously calculated abrasion rate, after a sputtered time of 5000s, is equivalent for the bulk and for the sample surface (including the oxide).

Figure 8: Distribution of Fe, Cr, Ni and Mo components within the passive film formed on 316L stainless steel in deaerated borate buffer solution at -0.1 V_{SCE} (a) for an uncharged specimen, (b) for a hydrogen cathodically charged specimen.

The distribution of the different components within the passive layer is mainly similar before and after hydrogen ingress. In fact, each sample has a passive layer with few differences in the oxide composition. A weak increase in the Fe II/Fe III ratio could be noticed after cathodic charging (from 0.74 to 0.97) as well as a slight increase of the $Cr^{3+}_{hydroxide}$/ Cr^{3+}_{oxide} ratio (from 0.72 to 0.83). Finally, a small diminution of the contribution of Cr-oxide and Cr-hydroxide (from 17% to 14% of the total atomic composition including underlying contribution) to the total surface signal (before ion sputtering) is observed after cathodic charging. Figure 8 also allows to compare the thicknesses of the passive films formed on uncharged and cathodically charged specimens. Two verticals lines indicate the minimal and maximal thicknesses that can be evaluated on the base of XPS measurements. It is obvious that cathodic charging does not seem to markedly influence the thickness of the passive film, which can be roughly evaluated between 1 and 2 nm in agreement with EIS measurements.

All the XPS results suggest few variations in the composition and thickness of the passive layer. The modification of the Fe[II]/Fe[III] ratio as well as Cr-oxide and Cr hydroxide

concentrations looks relevant with other results in the literature [23, 65–67]. However, it must be noticed that as XPS experiments are ex-situ, and as the passive film can be modified in dry or vacuum environments, these results are only indicative.

3.6 Mott-Schottky Analysis

Generally, a semiconductor behavior could be used to describe the properties of the passive films of stainless steels, which can be evaluated using Mott-Schottky analysis. Based on the Mott-Schottky theory, for a passive film of a stainless steel, the capacity of the spaced charge layer is much smaller than the capacity of the Helmholtz layer which may be neglected. In addition, considering the inverse square of the space charge capacitance follows a linear relationship with the applied potential, the space charge capacitance may be linked to donor or acceptor densities using the following equations [68, 69]:

$$\frac{1}{C^2} = \frac{2}{\varepsilon\varepsilon_0 q N_D}\left(E - E_{FB} - \frac{kT}{q}\right) for\ n-type \quad (7)$$

$$\frac{1}{C^2} = \frac{2}{\varepsilon\varepsilon_0 q N_A}\left(E_{FB} - E - \frac{kT}{q}\right) for\ p-type \quad (8)$$

where N_D and N_A are the donor and acceptor densities (cm^{-3}), respectively, q is the elementary charge, k is the Boltzmann constant and T is the temperature in Kelvin (K). ε and ε_0 are the dielectric constant of the material (15.6) and the permittivity of vacuum (8.85×10^{-14} $F.cm^{-1}$) respectively, E is the applied potential, and E_{FB} is the flat band potential which can be determined from the intercept with the E axis of the linear region of the plot $1/C^2$ against E.

Mott-Schottky tests were conducted on uncharged, charged and 168h desorbed samples after 1h of passivation in borate buffer solution. Figure 9 presents representative Mott-Schottky plots obtained at 1 kHz as well as the corresponding equations of the linear regions.

Figure 9: Mott-Schottky plots obtained on AISI 316L stainless steel at 1 kHz in deaerated borate buffer solution for an uncharged, 72h charged and 168h desorbed specimens.

Figure 9 shows roughly identical behaviors before and after hydrogen ingress. The only difference is a noisier signal after cathodic charging. The linear region comprised between -0.1V_{SCE} and 0.3V_{SCE} presents a positive slope that illustrates the electronic behavior of a n-type semiconductor, whose predominant dopant species should presumably be oxygen vacancies and/or cation interstitials. The donor densities are calculated using equation (7) from the slope of the linear regions and are 8.0±0.7 10^{20} cm^{-3}, 7.7±0.1 10^{20} cm^{-3} and 8.1±0.6 10^{20} cm^{-3} for the uncharged, 72h charged and 168h desorbed samples respectively. These values are in good agreement with the literature on passive films formed on austenitic stainless steel at ambient temperature [13–15, 70]. Even if some studies attest a modification of donor densities by Mott-Schottky after hydrogen ingress on AISI 304 [13], AISI 310 [14] and wrought AISI 316L [46, 71], such evolution has not been observed in this study.

4. Discussion

4.1 Effect of mobile hydrogen on anodic processes

Our approach which combined global and local experimental tools allowed to estimate that at the end of the hydrogen charging process, the local concentration of hydrogen in AISI 316L, due to a gradient of concentration distributed on 76 µm, was about 530 wppm [24]. A part of absorbed hydrogen is rapidly released during desorption, then it remains a total hydrogen concentration of approximatively 16 ± 7 wppm leading to a local concentration estimated around 105 wppm. In a second time, the study of hydrogen desorption, which is one of the originalities of this work, allows to enlighten the role of mobile hydrogen on the

electrochemical behavior. It is important to note that this work does not allows to distinguish the role of the concentration of mobile hydrogen with the role of the flux of mobile hydrogen desorption, which will be the topic of future works.

The high hydrogen concentration leads to modifications of the electrochemical behavior of the stainless steel. In fact, potentiodynamic tests show an increase in the surface reactivity due to hydrogen absorption. In potentio-dynamic tests, the current density detected at -0.1 V_{SCE} increases from 1.1 $\mu A.cm^{-2}$ to 4.0 $\mu A.cm^{-2}$ after cathodic charging. This effect is even higher in stationary conditions as current density at steady stage during potentiostatic tests increases from 0.18 $\mu A.cm^{-2}$ to 2.68 $\mu A.cm^{-2}$ after cathodic charging. This increase in intensity attests a higher surface reactivity and a less protective passive film. Using high field model, we showed that the current density attributed to the passive layer growth is not significantly modified after charging whereas the contribution of other anodic processes strongly increases (cf. Figure 4 and Table 3). These processes, which can be due to the modification of the passive layer after hydrogen absorption and/or modifications of local electrolyte during hydrogen desorption, are probably led by passive film dissolution and/or hydrogen oxidation. Previous work, conducted on stainless steels, already attest an increase in dissolution kinetics in neutral solution with hydrogen absorption [4, 14].

On the other hand, the desorption of mobile hydrogen induces a reduction of the passive current densities, so of the surface reactivity, as attests the Figure 10-a for the potentiodynamic tests and Figure 10-b for the potentiostatic tests.

Figure 10: (a) Evolution of the passive current density with the local concentration of hydrogen from potentiodynamic tests. Different colors are used for the different desorption times: 24h (grey), 48h (orange),72h (green) and 168h (pink) (b) Evolutions of

the experimental steady state current (J_{SS} =squares), the calculated growth current ($J_{SSgrowth}$=crosses) and corrected anodic current (J_{SSca}=right Crosses) at steady state from potentiostatic tests with the local concentration of hydrogen (the color code is the same as in Figure 10-a).

Figure 10-a presents the evolution of the passive current density from potentiodynamic experiments with the local concentration of hydrogen and suggests a quasi-linear relation between mobile hydrogen concentration and passive current density. After one week of desorption a difference between the passive current of the desorbed sample and the uncharged sample persists. This difference could be attributed to irreversible effects such as trapped hydrogen or any microstructural modification induced by cathodic charging, for example, the formation of vacancies [6, 72, 73], dislocations [74, 75] or martensite [74–76]. However, Figure 10-a highlights that the main impacts on the passive current density can be attributed to mobile hydrogen. Figure 10-b plots the steady state current density (from potentiostatic tests) as well as the current density of film growth ($J_{SSgrowth}$) and the corrected anodic current density (J_{SSca}) versus the local hydrogen concentration. A quasi-linear relationship between mobile hydrogen and the steady state passive current density can be observed. Moreover, after more than 2 days of desorption, even if the local H concentration is around 100 wppm, the stationary current density is very close to that for the uncharged specimen. This suggests a totally reversible effect on current density at steady state due to hydrogen desorption and thereby this supports the assumption of a main impact due to mobile hydrogen. The difference between the partial reversibility of the potentiodynamic tests and total reversibility of the potentiostatic tests is currently not explained. Figure 10-b also highlights that mobile hydrogen strongly modifies the corrected anodic current and has a low impact on passive layer growth. This analysis is supported with XPS results where few differences were noticed on the thickness and chemical composition of the oxide layer formed before and after

hydrogen absorption. Corrected anodic current includes all anodic processes besides the film growth. This current is probably linked with dissolution and, for a charged sample, with hydrogen oxidation. As it was previously shown, cathodic charging induces a high hydrogen concentration under the metallic surface. Hydrogen could be oxidized at the metal-film interface then H^+ could be extracted by the high electric field, or hydrogen could diffuse from bulk to passive film surface and could then be oxidized in H^+ at film-electrolyte interface. In both cases, this should increase the current density [7, 22, 77] and can also decrease the interfacial pH making the film more prone to dissolution and breakdown [4, 5, 7, 65, 70, 78]. At this point, it is impossible to clearly determine the contributions of dissolution and hydrogen oxidation to the current density of the anodic process. The increase of dissolution kinetics could be due to many factors such as defect formation due to hydrogen absorption [3, 4, 13, 66, 70, 71, 79], lattice or structural modification [22, 80] or even a local acidification of the electrolyte due to the desorption of a proton [4, 5, 65, 70, 79, 80]. This last assumption is supported by the partial reversibility which can be linked to a smaller quantity of desorbed hydrogen during the electrochemical test after a long desorption time. Moreover, electrochemistry impedance spectroscopy suggests a decrease in passive layer properties. The EIS results, presented in this work, suggest an important drop of the oxide resistance after cathodic charging (from 15.1×10^5 to 1.64×10^5 Ohm.cm²), in agreement with the results obtained by Ninghsen *et al.* on 316L in borate buffer after hydrogen absorption [4]. This phenomenon could be attributed to many factors as modification of the thickness or composition of the oxide layer or the formation of defects in the passive film. Figure 11 presents the evolution of the oxide resistance as a function of the hydrogen concentration during the desorption of mobile hydrogen. The resistance increases with desorption time, highlighting the effect of mobile hydrogen on passive layer behavior. After a desorption time of 168h, the initial resistance is not totally recovered, indicating a weak irreversible effect

which could be attributed to trapped hydrogen or microstructural modifications. XPS and EIS results do not attest to a thickness alteration and few chemical modifications have been noticed. The film capacitance (obtained with equation (4)) presents low variations, especially with the incertitude related to the deduction of this capacity from a CPE. The equation (6), previously defined, gives a relation between oxide capacity and passive layer thickness, which seems comprised between 2.0 and 3.1 nm. This result is in agreement with the XPS analysis where film thickness seems not be affected by hydrogen. In addition, the solution resistance (R_S), the charge transfer resistance (R_1) and the double layer capacitance (C_1), do not appear to be affected by cathodic charging.

Figure 11: Evolution of EIS oxide resistance parameter obtained by fitting with equivalent electrical circuit in function of hydrogen desorption time with the 72h charged sample in red, and respectively the 24h, 48h,72h and 168h desorbed samples in grey, orange, green and pink.

4.2 Effect of hydrogen desorption on the point defect diffusivity inside the passive film

In this work, we show a strong impact of the hydrogen absorption on the electrochemical processes on the surface of an AISI 316L in borate buffer. Dynamic and static polarizations attest to an increase in the surface activity while the EIS results suggest a modification of some passive layer properties. On the contrary, Mott-Schottky tests suggest that the donor density (oxygen vacancies or interstitial cations) is not modified after hydrogen absorption. The mobility, D_0 of these charge carriers is a key point to understand the passive layer behavior [35, 81]. The Point Defect Model (PDM) has been used to explain, under stationary conditions, the growth, breakdown and conservation of the passive layer by the formation and transport of point defects [35, 82–85]. From PDM, the current density at steady state can be

described as depending on the flux of cations and oxygen vacancies using the following equation [84]:

$$J_{SS} = F\left[\eta J_M - 2\left(\frac{\eta}{\chi}\right)J_O\right] \quad (9)$$

with J_{SS} the current density at the steady state obtained by potentiostatic polarization (*cf.* Table 3), F the Faraday constant and η the charge of the cation ejected from the passive layer. χ represents the charge of cations in the form of oxide, J_M the flux of cation vacancies (from film/solution interface to metal/film interface) and J_O the flux of anionic vacancies (considering as oxygen vacancies in this study) [35].

Mott-Schottky tests suggest that passive layers have a n-type semiconductor behavior. Under this consideration, we assume that the charge transport is widely due to oxygen vacancies and/or interstitial cations, thereby enabling to neglect the cationic vacancies flux in the equation (9) [35, 81, 86, 87]. Considering the charge of dissolved cations and oxide cations are equal, the current density can be described with the following equation:

$$J_{SS} = -2FJ_O \quad (10)$$

Macdonald *et al.* [83, 84] describe, for a passive layer thicker than 0.2 nm, the anionic vacancies flux as:

$$J_O = -2KD_O N_D \quad (11)$$

with D_O the oxygen vacancies mobility, N_D the concentration of oxygen vacancies in mol (assuming here as equal to the donor density obtained by Mott-Schottky), and K a factor which depends on the electric field strength ($\bar{e}$), the Faraday constant, the temperature, and the gas constant:

$$K = \frac{F\bar{e}}{RT} \quad (12)$$

In this work, an electric field of 10^6 V.cm^{-1} was considered to describe the electric field of a passive layer, in accordance with several works [16, 35, 39, 70, 81, 87]. In addition, we consider that this field is identical before and after cathodic charging because the high field model, apply to potentiostatic polarization, suggests few modifications of the kinetics of the passive layer growth and, moreover, XPS analysis do not show a strong modification of the thickness and chemical composition [70]. Consequently, K is constant with a value of 3.9 x 10^6 at 25°C.

The current density at the steady state can be described as depending on the oxygen vacancies mobility by combining equation (10) and (11):

$$J_{SS} = 4FKD_O N_D \quad (13)$$

with J_{SS} the current density at steady state obtained during the passive layer formation at -0.1 V_{ECS} (*cf.* Table 3) and N_D the donor densities obtained by the Mott-Schottky analysis.

The resulting vacancies mobility are given in Table 5.

Table 5: Evolution of anionic vacancies mobility in the passive layer.

Samples	**J_{ss} (µA.cm^{-2})**	**N_D (10^{-3} mol)**	**D_O (10^{-17} cm².s^{-1})**
Uncharged	0.176 ± 0.002	1.33	0.90
72h Charged	2.682 ± 0.007	1.28	14.0
168h Desorbed	0.212 ± 0.001	1.35	1.0

First, for the uncharged sample, the mobility of the main charged carriers has been estimated to approximately 9.0 x 10^{-18} cm².s^{-1}, which is in good agreement with the literature. In fact, Wang *et al.* estimated, by Tof-SIMS, an anionic mobility through an oxide layer formed on an austenitic stainless steel AISI 304 comprised between 1.6 x 10^{-17} cm².s^{-1} and 2.0 x 10^{-17} cm².s^{-}

[1] [88]. In addition, Ahn and Kwon [35] obtained, thanks to the combination of current density at steady stage and Mott-Schottky analysis, a coefficient of mobility of oxygen vacancies comprised between 1.64 $x10^{-17}$ $cm^2.s^{-1}$ and 2.04 $x10^{-17}$ $cm^2.s^{-1}$ for a passive layer formed on iron in borate buffer. The results presented in Table 5, obtained thanks to equation (13), suggest a strong increase in the vacancies mobility up to 1.4 x 10^{-16} $cm^2.s^{-1}$ with hydrogen absorption. The increase in the mobility of oxygen vacancies after hydrogen absorption is explained by Zeng *et al.* [77] with the formation of a gradient of concentration of positively charged hydrogen ions in the passive layer. Indeed, they suppose that, during desorption, protons diffuse from the metal to the passive layer and then, their concentration drops at the film/solution interface. This gradient induces an additional electrical strength, which might be added to the electric field as a repulsive force to positive charge as Fe^{2+}, Cr^{3+} and oxygen vacancies, thus enhancing their migration [70, 77]. This analysis suggests that hydrogen absorption increases the mobility of anionic vacancies positively charged. The PDM suggests that a part of the current density is controlled by anionic vacancies flux. Consequently, an increase in this flux could partially explain the increase in current density observed after hydrogen absorption. However, this last analysis requires to consider that, after cathodic charging, under stationary conditions, all the current could be attributed to passive layer evolution (breakdown, growth, and conservation). However, a contribution of the current of hydrogen oxidation on the metal surface could not be excluded and should induce an overestimation of the anionic vacancies mobility after hydrogen absorption. This assumption will be studied further in future work.

5. Conclusion

This work attests to a strong effect of hydrogen absorption on the electrochemical processes, especially in the passive range, on an AISI 316L in borate buffer solution. Potentiodynamic

and potentiostatic polarization curves have been used to characterize the electrochemical behavior and attest to an increase in the surface reactivity, which can mostly be linked with an increase in dissolution kinetics and/or hydrogen oxidation. The EIS results suggest a modification of some passive layer properties, while XPS analyses do not show strong modifications. These results could be correlated with an increase in anionic vacancies mobility in the oxide film due to hydrogen absorption.

One of the main results of this work deals with the effect of mobile hydrogen on electrochemical behavior. The obtained results suggest, using different desorption times, that the increase in dissolution kinetics is mainly due to mobile hydrogen. Unfortunately, the effect of the flux of mobile hydrogen cannot be distinguished from the effect of its concentration and will be investigated in future work. In fact, the flux should induce interface modifications as local acidification of the electrolyte while the interstitial hydrogen should modified electronic properties and defects concentrations.

Ackowledgements

This work was supported by the Ministère de l'Enseignement Supérieur et de la Recherche. We are grateful to the *Placamat institute* from Bordeaux University for her assistance during XPS experiments. The GDOES experiment was performed at the CRM Group (Avenue du Bois Saint-Jean 21 P59 4000 Liège BELGIQUE) - our thanks to C. Brandt and A. Dupont. The authors wish to thank P. Jacques, S. Reuter and P. Eloy from the pole IMAP of the Catholic University of Louvain-la-Neuve (Place Sainte Barbe 2/L5.02.02 1348 Louvain-la-Neuve) for helpful discussions. We would also like to acknowledge our colleague C. Berziou for his contributions to the Hydrogen analyses facilities in our laboratory.

References

[1] Vanýsek P. Electrochemical Series. In: CRC Handbook of Chemistry and Physics. 89th ed. Chemical Rubber Company; 2008.

[2] Guedes D, Cupertino Malheiros L, Oudriss A, Cohendoz S, Bouhattate J, Creus J, et al. The role of plasticity and hydrogen flux in the fracture of a tempered martensitic steel: A new design of mechanical test until fracture to separate the influence of mobile from deeply trapped hydrogen. Acta Materialia. 2020;186:133–48.

[3] Ningshen S, Mudali UK, Amarendra G, Gopalan P, Dayal RK, Khatak HS. Hydrogen effects on the passive film formation and pitting susceptibility of nitrogen containing type 316L stainless steels. Corrosion Science. 2006;48:1106–21.

[4] Ningshen S, Mudali UK. Hydrogen effects on pitting corrosion and semiconducting properties of nitrogen-containing type 316L stainless steel. Electrochimica Acta. 2009;54[26]:6374–82.

[5] Ejaz A, Lu Z, Chen J, Xiao Q, Ru X, Han G, et al. The effects of hydrogen on anodic dissolution and passivation of iron in alkaline solutions. Corrosion Science. 2015;101:165–81.

[6] Fukai Y. The Metal-Hydrogen System. Springer; 2005.

[7] Thomas S, Ott N, Schaller RF, Yuwono JA, Volovitch P, Sundararajan G, et al. The effect of absorbed hydrogen on the dissolution of steel. Heliyon. 2016;2[12]:25.

[8] Turnbull A. Hydrogen diffusion and trapping in metals. In: Gaseous Hydrogen Embrittlement of Materials in Energy Technologies [Internet]. Elsevier; 2012 [cited 2020 Aug 26]. p. 89–128. Available from: https://linkinghub.elsevier.com/retrieve/pii/B9780857095367500040

[9] Feaugas X. On the origin of the tensile flow stress in the stainless steel AISI 316L at 300 K: back stress and effective stress. Acta Materialia. 1999;47[13]:3617–32.

[10] Martin F, Feaugas X, Oudriss A, Tanguy D, Briottet L, Kittel J. Chapter 8. State of Hydrogen in Matter: Fundamental Ad/Absorption, Trapping and Transport Mechanisms. In: "Mechanics - Microstructure - Corrosion" Coupling. Christine Blanc ans Isabelle Aubert. ISTE; 2018. p. 171–197.

[11] Ramasubramanian N. Analysis of Passive Films on Stainless Steel by Cyclic Voltammetry and Auger Spectroscopy. J Electrochem Soc. 1985;132[4]:793.

[12] Kocijan A, Donik Č, Jenko M. Electrochemical and XPS studies of the passive film formed on stainless steels in borate buffer and chloride solutions. Corrosion Science. 2007;49[5]:2083–98.

[13] Yang Q, Luo JL. The hydrogen-enhanced effects of chloride ions on the passivity of type 304 stainless steel. Electrochimica Acta. 2000;45[24]:3927–37.

[14] Yang MZ, Luo JL, Yang Q, Qiao LJ, Qin ZQ, Norton PR. Effects of Hydrogen on Semiconductivity of Passive Films and Corrosion Behavior of 310 Stainless Steel. Journal of The Electrochemical Society. 1999;146:2107–12.

[15] Yang MZ, Yang Q, Luo JL. Effects of hydrogen on passive film and corrosion of AISI 310 stainless steel. Corrosion Science. 1999;41:741–5.

[16] Xu H, Sun D, Yu H. Repassivation behavior of 316L stainless steel in borate buffer solution: Kinetics analysis of anodic dissolution and film formation. Applied Surface Science. 2015;357:204–13.

[17] Hakiki NB, Boudin S, Rondot B, Da Cunha Belo M. The electronic structure of passive films formed on stainless steels. Corrosion Science. 1995;37[11]:1809–22.

[18] Ge H-H, Xu X-M, Zhao L, Song F, Shen J, Zhou G-D. Semiconducting behavior of passive film formed on stainless steel in borate buffer solution containing sulfide. J Appl Electrochem. 2011;41[5]:519–25.

[19] Nicic I, Macdonald DD. The passivity of Type 316L stainless steel in borate buffer solution. Journal of Nuclear Materials. 2008;379[1–3]:54–8.

[20] Oh K, Ahn S, Eom K, Jung K, Kwon H. Observation of passive films on Fe–20Cr–xNi (x=0, 10, 20wt.%) alloys using TEM and Cs-corrected STEM–EELS. Corrosion Science. 2014;79:34–40.

[21] Qiao L, Mao X. Thermodynamic analysis on the role of hydrogen in anodic stress corrosion cracking. Acta metallurgica mater. 1995;43[11]:4001–6.

[22] Qiao LJ, Luo JL. Hydrogen-Facilitated Anodic Dissolution of Austenitic Stainless Steels. Corrosion. 1998;54[4]:281–8.

[23] Shubina Helbert V, Nazarov A, Vucko F, Rioual S, Thierry D. Hydrogen effect on the passivation and crevice corrosion initiation of AISI 304L using Scanning Kelvin Probe. Corrosion Science. 2021 Apr;182:109225.

[24] Duportal M, Oudriss A, Feaugas X, Savall C. On the estimation of the diffusion coefficient and distribution of hydrogen in stainless steel. Scripta Materialia. 2020;186:282–6.

[25] Yashiro H, Pound B, Kumagai N, Tanno K. The effect of permeated hydrogen on the pitting of 304 stainless steel. Corrosion Science. 1998;40[4/5]:781–91.

[26] Feaugas X, Gaudin C. Ratchetting process in the stainless steel AISI 316L at 300 K: an experimental investigation. International Journal of Plasticity. 2004;20[4–5]:643–62.

[27] Akiyama E, Li S. Electrochemical hydrogen permeation tests under galvanostatic hydrogen charging conditions conventionally used for hydrogen embrittlement study. Corrosion Reviews. 2015;11.

[28] Shintani D, Ishida T, Izumi H, Fukutsuka T, Matsuo Y, Sugie Y. XPS studies on passive film formed on stainless steel in a high-temperature and high-pressure methanol solution containing chloride ions. Corrosion Science. 2008;50:2840–5.

[29] Cui Z, Chen S, Dou Y, Han S, Wang L, Man C, et al. Passivation behavior and surface chemistry of 2507 super duplex stainless steel in artificial seawater: Influence of dissolved oxygen and pH. Corrosion Science. 2019;150:218–34.

[30] Olefjord I. Surface Composition of Stainless Steels during Anodic Dissolution and Passivation Studied by ESCA. J Electrochem Soc. 1985;132[12]:2854.

[31] Moulder JF, Stickle WF, Sobol EP, Bomben KD. Handbook of X-Ray Photoelectron Spectroscopy. Jill Chastain. Perkin-Elmer Corporation; 1992.

[32] De Vito E, Marcus P. XPS study of passive films formed on molybdenum-implanted austenitic stainless steels. Surf Interface Anal. 1992;19[1–12]:403–8.

[33] Biesinger MC, Brown C, Mycroft JR, Davidson RD, McIntyre NS. X-ray photoelectron spectroscopy studies of chromium compounds. Surf Interface Anal. 2004;36[12]:1550–63.

[34] Brass A-M, Chêne J. Hydrogen uptake in 316L stainless steel: Consequences on the tensile properties. Corrosion Science. 2006;48[10]:3222–42.

[35] Ahn SJ, Kwon HS. Effects of solution temperature on electronic properties of passive film formed on Fe in pH 8.5 borate buffer solution. Electrochimica Acta. 2004;49[20]:3347–53.

[36] Cheng YF, Luo JL. Passivity and pitting of carbon steel in chromate solutions. Electrochimica Acta. 1999;44[26]:4795–804.

[37] Lutton K, Scully JR. Kinetics of Oxide Growth of Passive Films on Transition Metals. In: Encyclopedia of Interfacial Chemistry [Internet]. Elsevier; 2018 [cited 2020 May 2]. p. 284–90. Available from: https://linkinghub.elsevier.com/retrieve/pii/B9780124095472135760

[38] Cho E-A, Kim C-K, Kim J-S, Kwon H-S. Quantitative analysis of repassivation kinetics of ferritic stainless steels based on the high field ion conduction model. Electrochimica Acta. 2000;45[12]:1933–42.

[39] Cabrera N. Theory of the oxidation of metals. Reports on Progress in Physics. 1949;12[1]:163–84.

[40] Stellwag B. The mechanism of oxide film formation on austenitic stainless steels in high temperature water. Corrosion Science. 1998;40[2/3]:337–70.

[41] Qiao YX, Zheng YG, Ke W, Okafor PC. Electrochemical behaviour of high nitrogen stainless steel in acidic solutions. Corrosion Science. 2009;51[5]:979–86.

[42] Lee J-B. Effects of alloying elements, Cr, Mo and N on repassivation characteristics of stainless steels using the abrading electrode technique. Materials Chemistry and Physics. 2006;99[2–3]:224–34.

[43] Engseth P, Scully JC. Repassivation studies on an austenitic stainless steel in chloride solutions. Corrosion Science. 1975;15[6–12]:505–19.

[44] Escrivà-Cerdán C, Blasco-Tamarit E, García-García DM, García-Antón J, Akid R, Walton J. Effect of temperature on passive film formation of UNS N08031 Cr–Ni alloy in phosphoric acid contaminated with different aggressive anions. Electrochimica Acta. 2013;111:552–61.

[45] Fernández-Domene RM, Blasco-Tamarit E, García-García DM, García-Antón J. Cavitation corrosion and repassivation kinetics of titanium in a heavy brine LiBr solution evaluated by using electrochemical techniques and Confocal Laser Scanning Microscopy. Electrochimica Acta. 2011;58:264–75.

[46] Duan Z, Man C, Dong C, Cui Z, Kong D, wang L, et al. Pitting behavior of SLM 316L stainless steel exposed to chloride environments with different aggressiveness: Pitting mechanism induced by gas pores. Corrosion Science. 2020;167:108520.

[47] Orazem ME, Frateur I, Tribollet B, Vivier V, Marcelin S, Pébère N, et al. Dielectric Properties of Materials Showing Constant-Phase-Element (CPE) Impedance Response. J Electrochem Soc. 2013;160[6]:C215–25.

[48] Hirschorn B, Orazem ME, Tribollet B, Vivier V, Frateur I, Musiani M. Constant-Phase-Element Behavior Caused by Resistivity Distributions in Films. Journal of The Electrochemical Society. 2010;157[12]:458–63.

[49] Hirschorn B, Orazem ME, Tribollet B, Vivier V, Frateur I, Musiani M. Determination of effective capacitance and film thickness from constant-phase-element parameters. Electrochimica Acta. 2010;55[21]:6218–27.

[50] Abreu CM, Cristóbal MJ, Losada R, Nóvoa XR, Pena G, Pérez MC. High frequency impedance spectroscopy study of passive films formed on AISI 316 stainless steel in alkaline medium. Journal of Electroanalytical Chemistry. 2004;572[2]:335–45.

[51] Cui Z, Wang L, Ni H, Hao W, Man C, Chen S, et al. Influence of temperature on the electrochemical and passivation behavior of 2507 super duplex stainless steel in simulated desulfurized flue gas condensates. Corrosion Science. 2017;118:31–48.

[52] Benoit M, Bataillon C, Gwinner B, Miserque F, Orazem ME, Sánchez-Sánchez CM, et al. Comparison of different methods for measuring the passive film thickness on metals. Electrochimica Acta. 2016;201:340–7.

[53] Kocijan A, Merl DK, Jenko M. The corrosion behaviour of austenitic and duplex stainless steels in artificial saliva with the addition of fluoride. Corrosion Science. 2011;53[2]:776–83.

[54] Boissy C, Ter-Ovanessian B, Normand B. Correlation between predictive and descriptive models to characterize the passive film – Study of pure chromium by electrochemical impedance spectroscopy. Electrochimica Acta. 2015;174:430–7.

[55] Sun H, Wu X, Han E-H. Effects of temperature on the oxide film properties of 304 stainless steel in high temperature lithium borate buffer solution. Corrosion Science. 2009 Dec;51[12]:2840–7.

[56] Mohammadi F, Nickchi T, Attar MM, Alfantazi A. EIS study of potentiostatically formed passive film on 304 stainless steel. Electrochimica Acta. 2011;56[24]:8727–33.

[57] Yin Q, Kelsall GH, Vaughan DJ, Brandon NP. Mathematical Models for Time-Dependent Impedance of Passive Electrodes. J Electrochem Soc. 2001;148[3]:A200.

[58] Freire L, Carmezim MJ, Ferreira MGS, Montemor MF. The passive behaviour of AISI 316 in alkaline media and the effect of pH: A combined electrochemical and analytical study. Electrochimica Acta. 2010;55[21]:6174–81.

[59] Ge H-H, Zhou G-D, Wu W-Q. Passivation model of 316 stainless steel in simulated cooling water and the effect of sulfide on the passive film. Applied Surface Science. 2003;211[1–4]:321–34.

[60] Boudinar Y, Belmokre K, Touzet M, Devos O, Puiggali M. Investigation of the passivation process of plastically deformed 316L stainless steel using the high frequency capacitance obtained by EIS. Materials and Corrosion. 2019;70[2]:206–15.

[61] Córdoba-Torres P, Mesquita TJ, Devos O, Tribollet B, Roche V, Nogueira RP. On the intrinsic coupling between constant-phase element parameters α and Q in electrochemical impedance spectroscopy. Electrochimica Acta. 2012;72:172–8.

[62] Hirschorn B, Orazem ME, Tribollet B, Vivier V, Frateur I, Musiani M. Constant-Phase-Element Behavior Caused by Resistivity Distributions in Films. Journal of The Electrochemical Society. 2010;157[12]:C452–7.

[63] Ferreira MJJ, Cunha Belo M da. Influence of the Chemical Composition of Stainless Steels on the Electronic Structure of Passive Films Formed in Artificial Sea Water. Portugaliae Electrochimica Acta. 2004;22:263–78.

[64] Olsson C-OA, Landolt D. Passive films on stainless steels-chemistry, structure and growth - Olsson.pdf. Electrochimica Acta. 2003;48:1093–104.

[65] Yu JG, Luo JL, Norton PR. Electrochemical investigation of the effects of hydrogen on the stability of the passive film on iron. Electrochimica Acta. 2002;47[10]:1527–36.

[66] Yu JG, Zhang CS, Luo JL, Norton PR. Investigation of the Effect of Hydrogen on the Passive Film on Iron by Surface Analysis Techniques. J Electrochem Soc. 2003;150[2]:B68–75.

[67] Nazarov A, Vucko F, Thierry D. Scanning Kelvin Probe for detection of the hydrogen induced by atmospheric corrosion of ultra-high strength steel. Electrochimica Acta. 2016;216:130–9.

[68] Gelderman K, Lee L, Donne SW. Using the Mott–Schottky Equation. Journal of Chemical Education. 2007;84[4]:685–8.

[69] Quarto FD, Santamaria M. Semiconductor electrochemistry approach to passivity and passivity breakdown of metals and metallic alloys. Corrosion Engineering Science and Technology. 2004;39[1]:12.

[70] Wang X-Z, Luo H, Luo J-L. Effects of hydrogen and stress on the electrochemical and passivation behaviour of 304 stainless steel in simulated PEMFC environment. Electrochimica Acta. 2019;293:60–77.

[71] Kong D, Dong C, Ni X, Zhang L, Luo H, Li R, et al. Superior resistance to hydrogen damage for selective laser melted 316L stainless steel in a proton exchange membrane fuel cell environment. Corrosion Science. 2020;166:108425.

[72] Bukonte L, Ahlgren T, Heinola K. Thermodynamics of impurity-enhanced vacancy formation in metals. Journal of Applied Physics. 2017;121[4]:045102.

[73] Metsue A, Oudriss A, Feaugas X. Hydrogen solubility and vacancy concentration in nickel single crystals at thermal equilibrium: New insights from statistical mechanics and ab initio calculations. Journal of Alloys and Compounds. 2016;656:555–67.

[74] Eliezer D. The behaviour of 316L stainless steel in hydrogen. J Mater Sci. 1984;19[5]:1540–7.

[75] Teus SM, Shyvanyuk VN, Gavriljuk VG. Hydrogen-induced γ→ε transformation and the role of ε-martensite in hydrogen embrittlement of austenitic steels. Materials Science and Engineering: A. 2008;497[1–2]:290–4.

[76] Tanino M, Komatsu H, Funaki S. Hydrogen induced martensitic transformation and twin formation in stainless steels. J Phys Colloques. 1982;43[C4]:C4-503-C4-508.

[77] Zeng YM, Luo JL, Norton PR. New Interpretation of the Effect of Hydrogen on the Ion Distributions and Structure of Passive Films on Microalloyed Steel. J Electrochem Soc. 2004;151[6]:B291.

[78] Thomas S, Sundararajan G, White PD, Birbilis N. The Effect of Absorbed Hydrogen on the Corrosion of Steels: Review, Discussion, and Implications. CORROSION. 2017 Apr;73[4]:426–36.

[79] Wallinder D, Hultquist G, Tveten B, Ho E. Hydrogen in chromium: influence on corrosion potential and anodic dissolution in neutral NaCl solution. Corrosion Science. 2001;43:1267–81.

[80] Gu B, Luo J, Mao X. Hydrogen-Facilitated Anodic Dissolution-Type Stress Corrosion Cracking of Pipeline Steels in Near-Neutral pH Solution. Corrosion. 1999;55[1]:96–106.

[81] Ahn S, Kwon H. Diffusivity of point defects in the passive film on Fe. Journal of Electroanalytical Chemistry. 2005;579[2]:311–9.

[82] Macdonald DD. The history of the Point Defect Model for the passive state: A brief review of film growth aspects. Electrochimica Acta. 2011;56:1761–72.

[83] Macdonald DD. The Point Defect Model for the Passive State. Journal of Electrochemical Society. 1992;139[12]:3434–99.

[84] Macdonald DD. Steady-State Passive Films. J Electrochem Soc. 1992;139[1]:170.

[85] Urquidi-Macdonald M. Theoretical Analysis of the Effects of Alloying Elements on Distribution Functions of Passivity Breakdown. J Electrochem Soc. 1989;136[4]:961.

[86] Kloppers MJ, Bellucci F, Latanision RM. Electronic Properties and Defect Structure of Fe and Fe-Cr Passive Films. Corrosion. 1992;48[3]:229–38.

[87] Cheng YF, Yang C, Luo JL. Determination of the diffusivity of point defects in passive films on carbon steel. Thin Solid Films. 2002;416[1–2]:169–73.

[88] Wang L, Voyshnis S, Seyeux A, Marcus P. Ion transport mechanisms in the passive film formed on 304L stainless steel studied by ToF-SIMS with 18O isotopic tracer. Corrosion Science. 2020;173:108779.

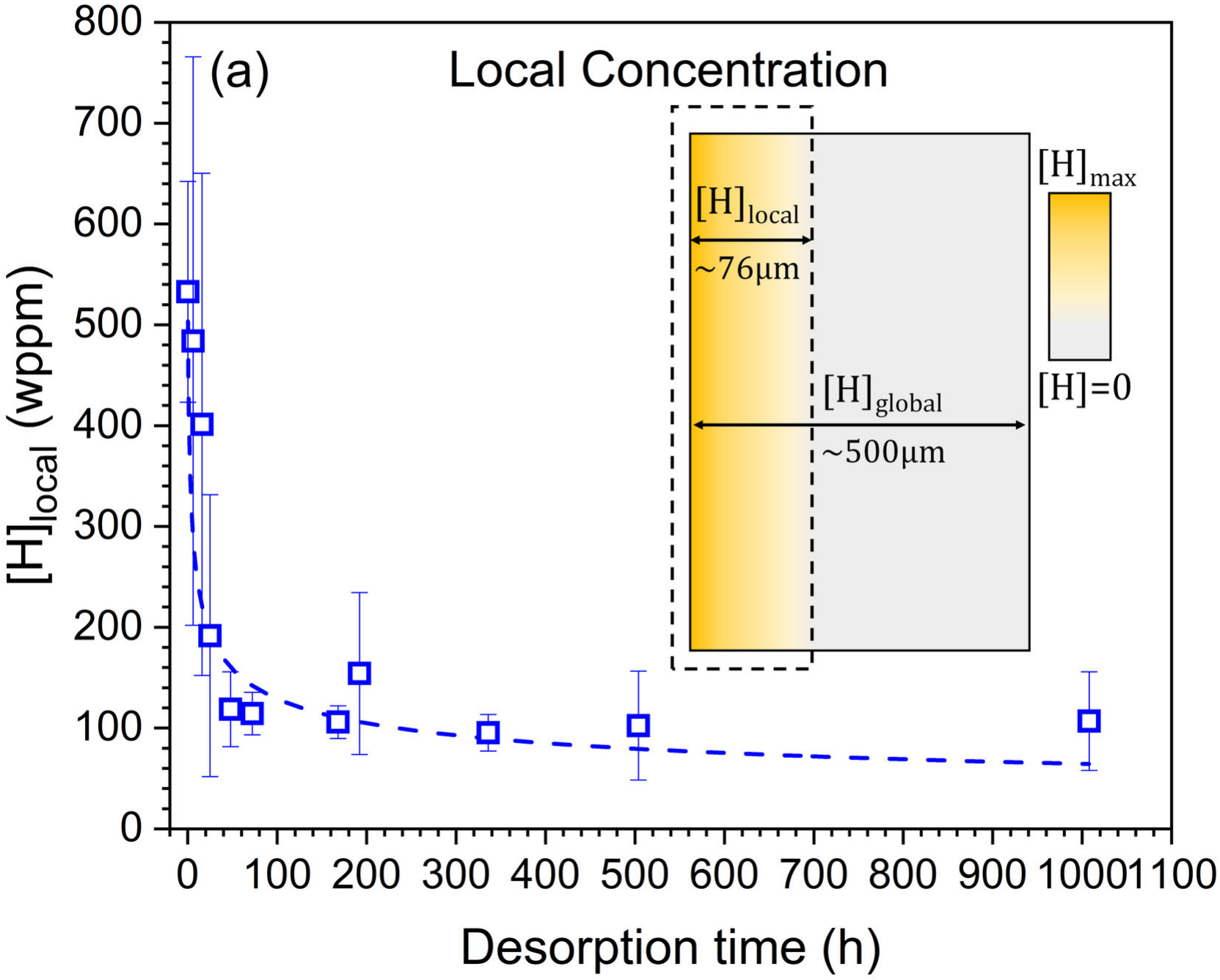
(a)
Local Concentration
[H]local (wppm)
Desorption time (h)
[H]local
~76μm
[H]global
~500μm
[H]max
[H]=0
0
100
200
300
400
500
600
700
800
900
1000
1100

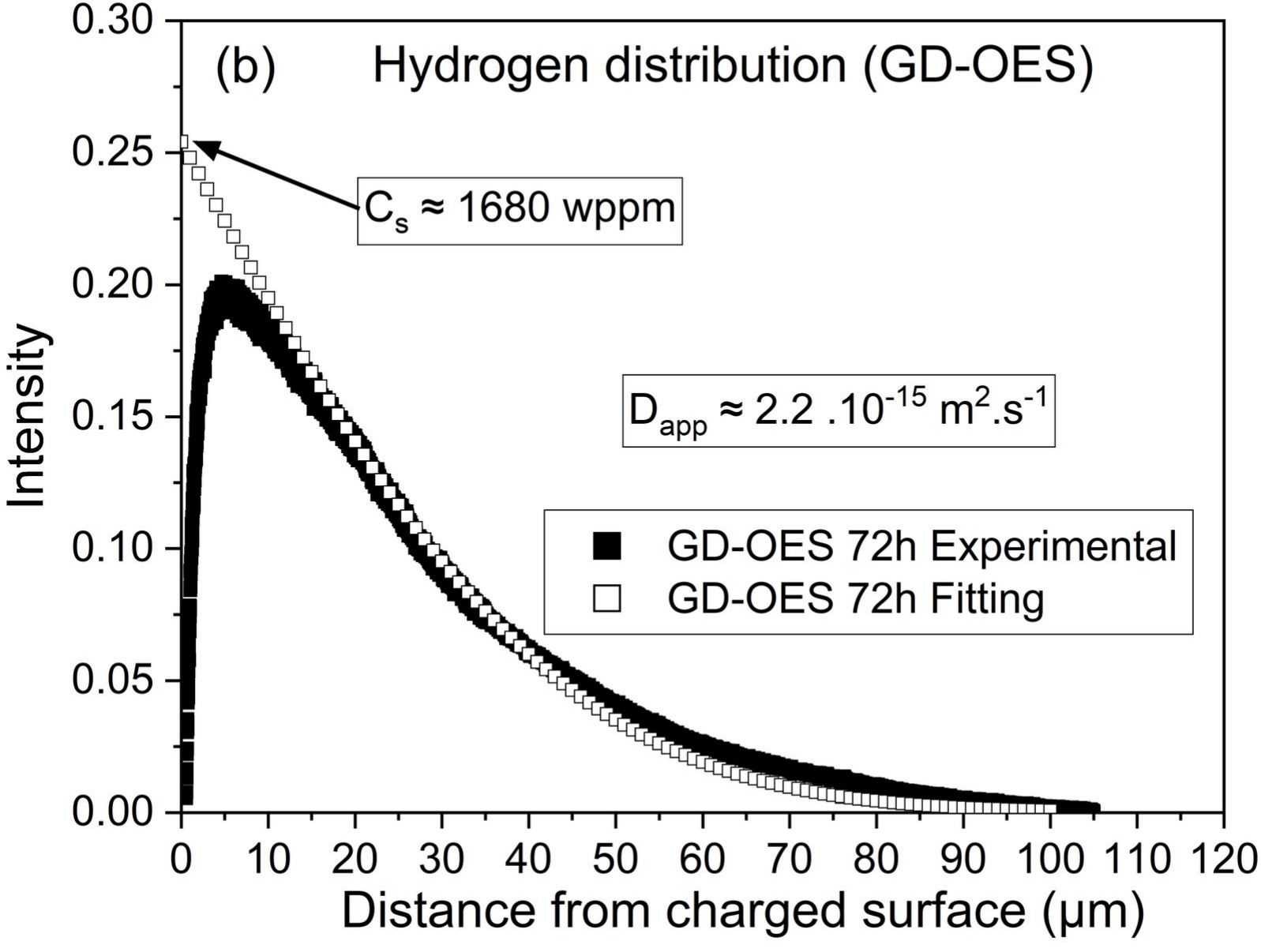
(b) Hydrogen distribution (GD-OES)
$C_s \approx 1680$ wppm
$D_{app} \approx 2.2 .10^{-15}$ m^2.s^{-1}
GD-OES 72h Experimental
GD-OES 72h Fitting
Intensity
Distance from charged surface (µm)
0.00
0.05
0.10
0.15
0.20
0.25
0.30
0
10
20
30
40
50
60
70
80
90
100
110
120

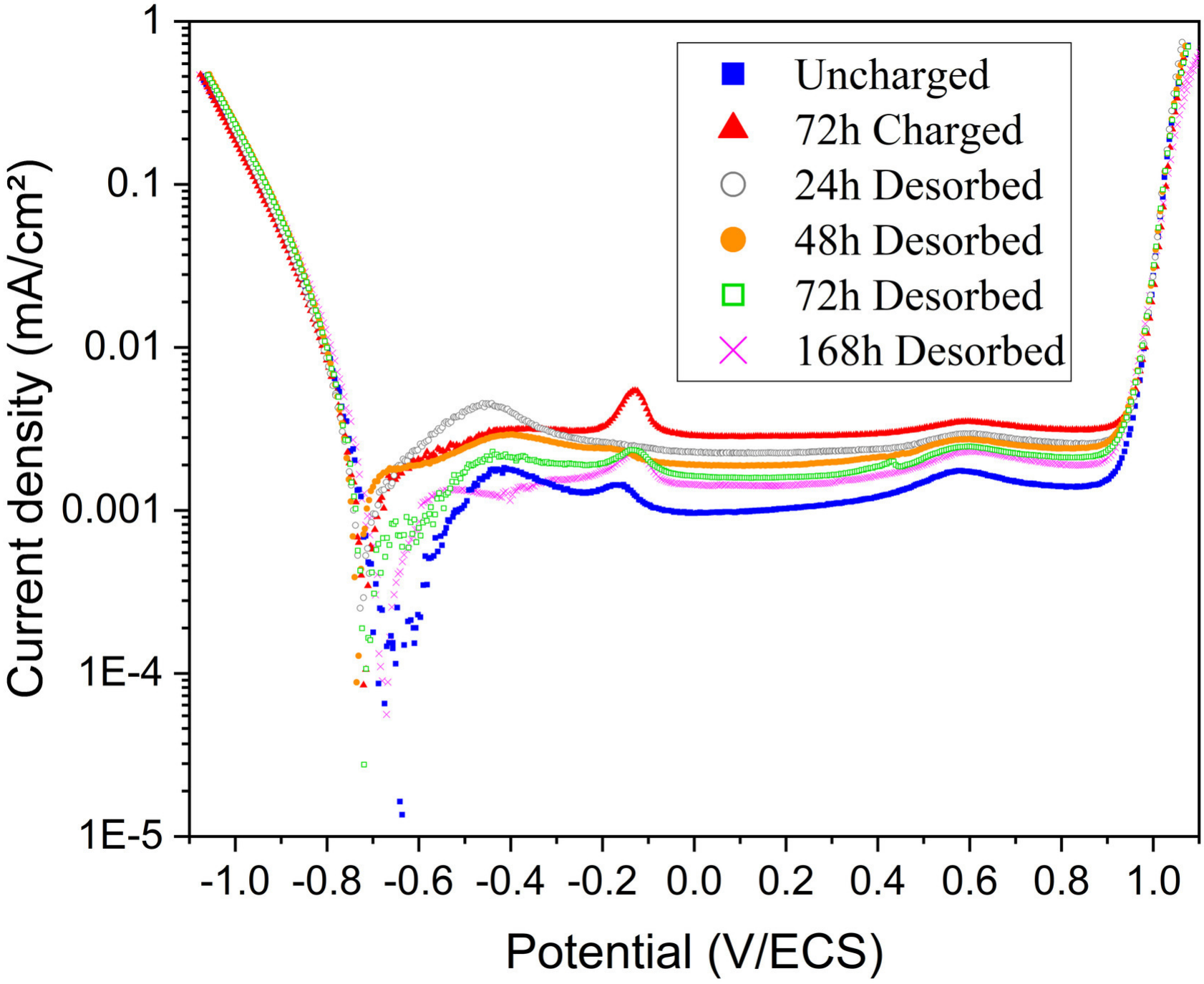
Uncharged
72h Charged
24h Desorbed
48h Desorbed
72h Desorbed
168h Desorbed
Current density (mA/cm²)
1
0.1
0.01
0.001
1E-4
1E-5
-1.0
-0.8
-0.6
-0.4
-0.2
0.0
0.2
0.4
0.6
0.8
1.0
Potential (V/ECS)

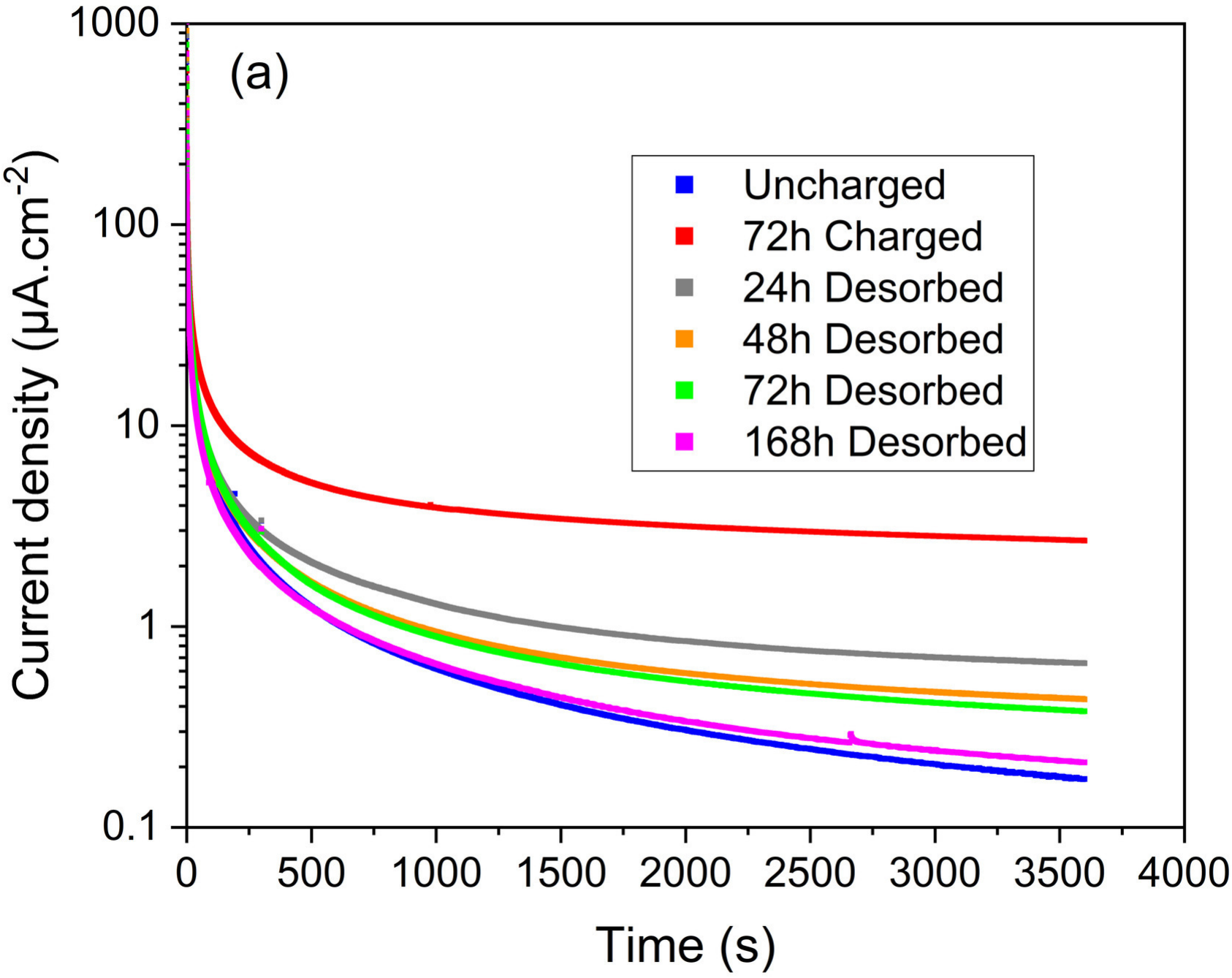
(a)
Uncharged
72h Charged
24h Desorbed
48h Desorbed
72h Desorbed
168h Desorbed
Current density (μA.cm-2)
Time (s)
1000
100
10
1
0.1
0
500
1000
1500
2000
2500
3000
3500
4000

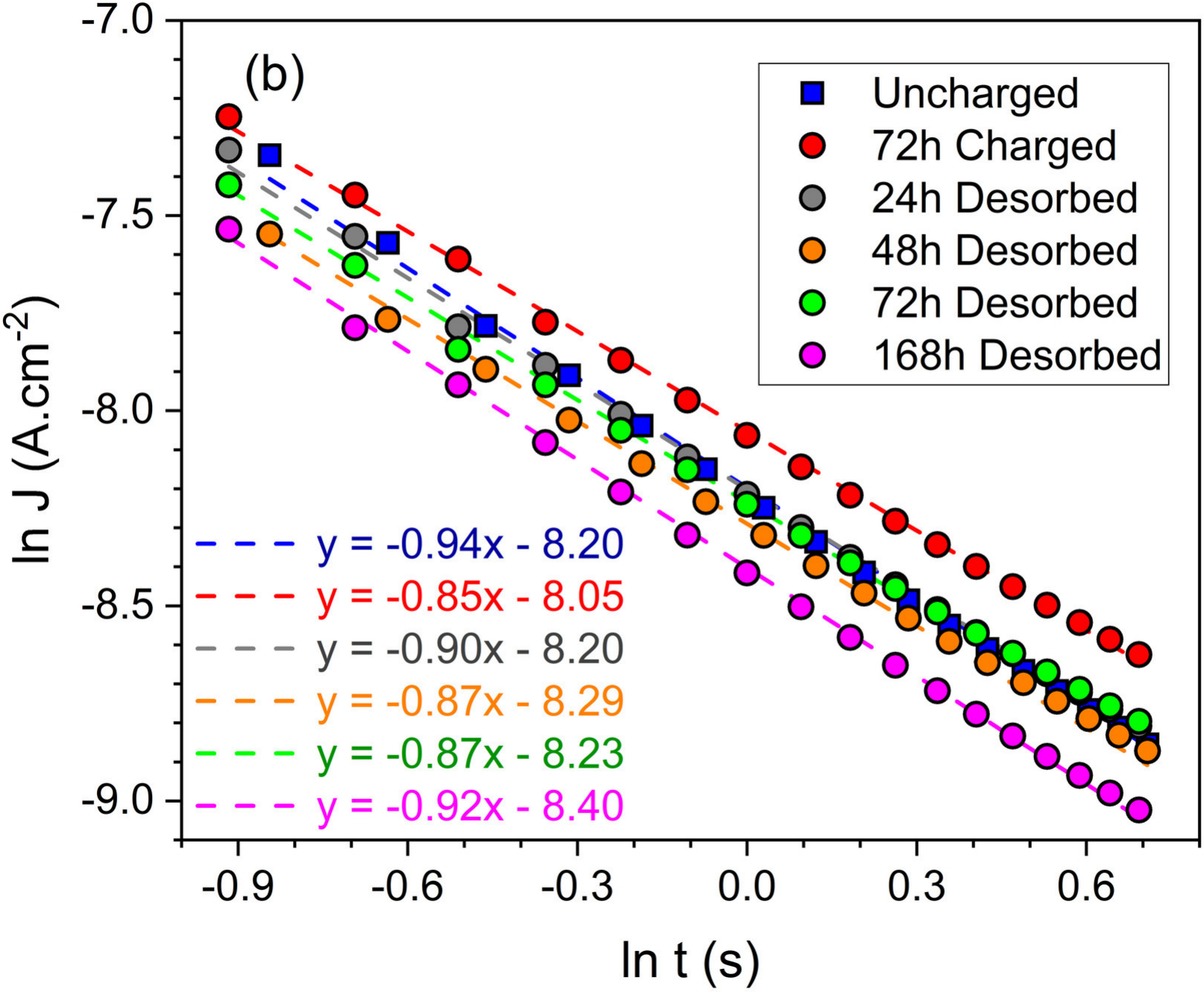
(b)
Uncharged
72h Charged
24h Desorbed
48h Desorbed
72h Desorbed
168h Desorbed
y = -0.94x - 8.20
y = -0.85x - 8.05
y = -0.90x - 8.20
y = -0.87x - 8.29
y = -0.87x - 8.23
y = -0.92x - 8.40
ln J (A.cm-2)
ln t (s)
-7.0
-7.5
-8.0
-8.5
-9.0
-0.9
-0.6
-0.3
0.0
0.3
0.6

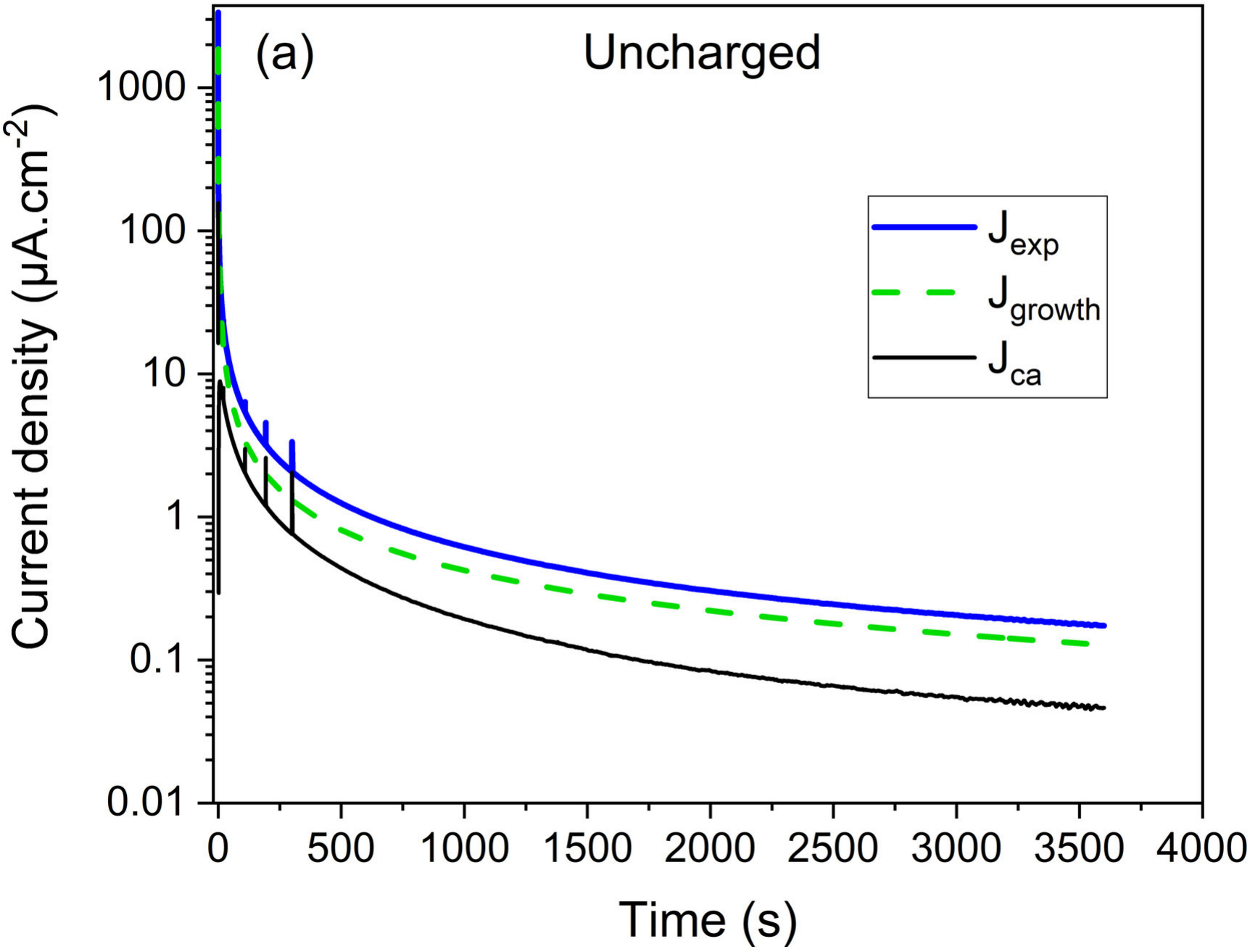
(a)
Uncharged
Current density (μA.cm-2)
1000
100
10
1
0.1
0.01
0
500
1000
1500
2000
2500
3000
3500
4000
Time (s)
Jexp
Jgrowth
Jca

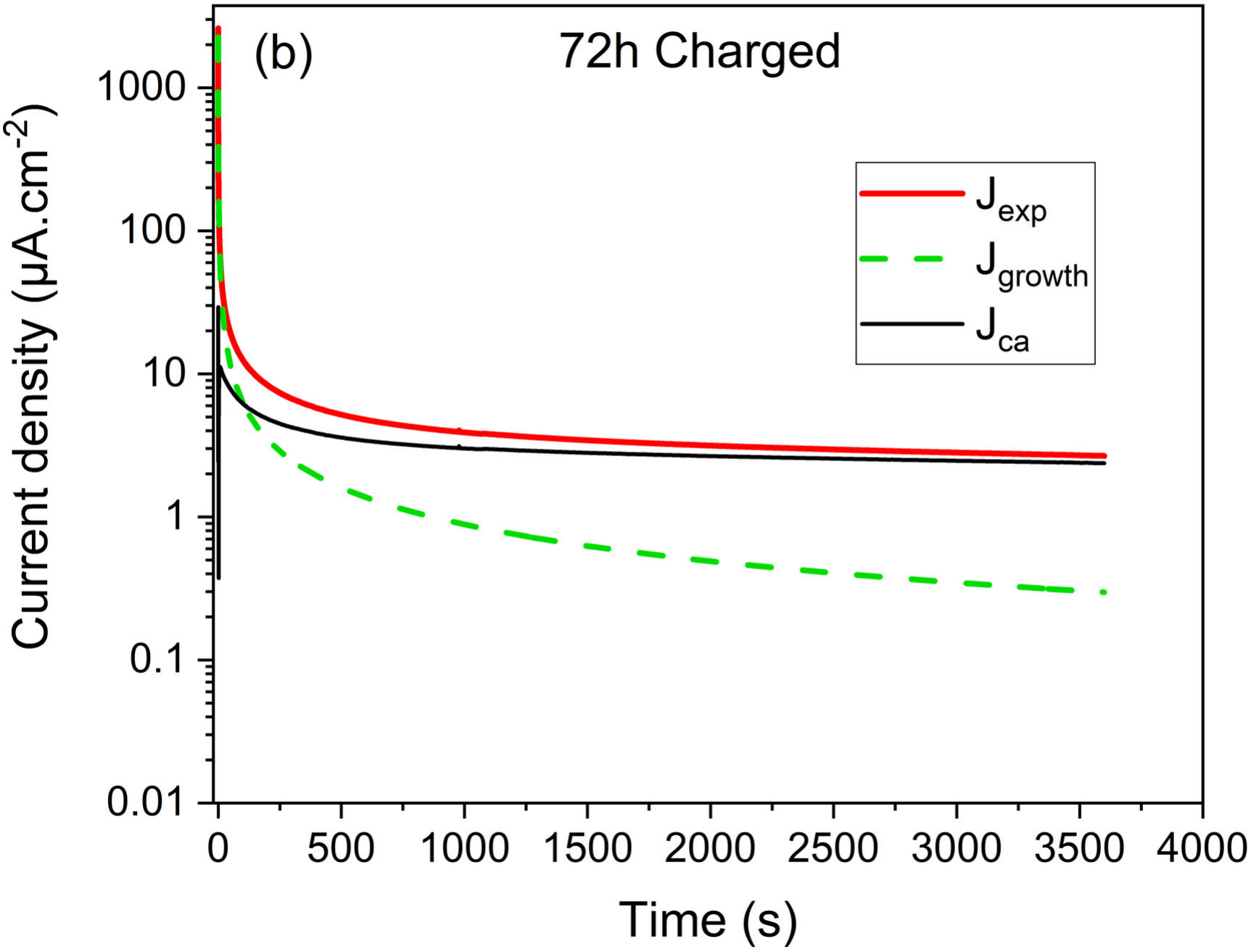
(b)
72h Charged
Current density (μA.cm-2)
1000
100
10
1
0.1
0.01
0
500
1000
1500
2000
2500
3000
3500
4000
Time (s)
Jexp
Jgrowth
Jca

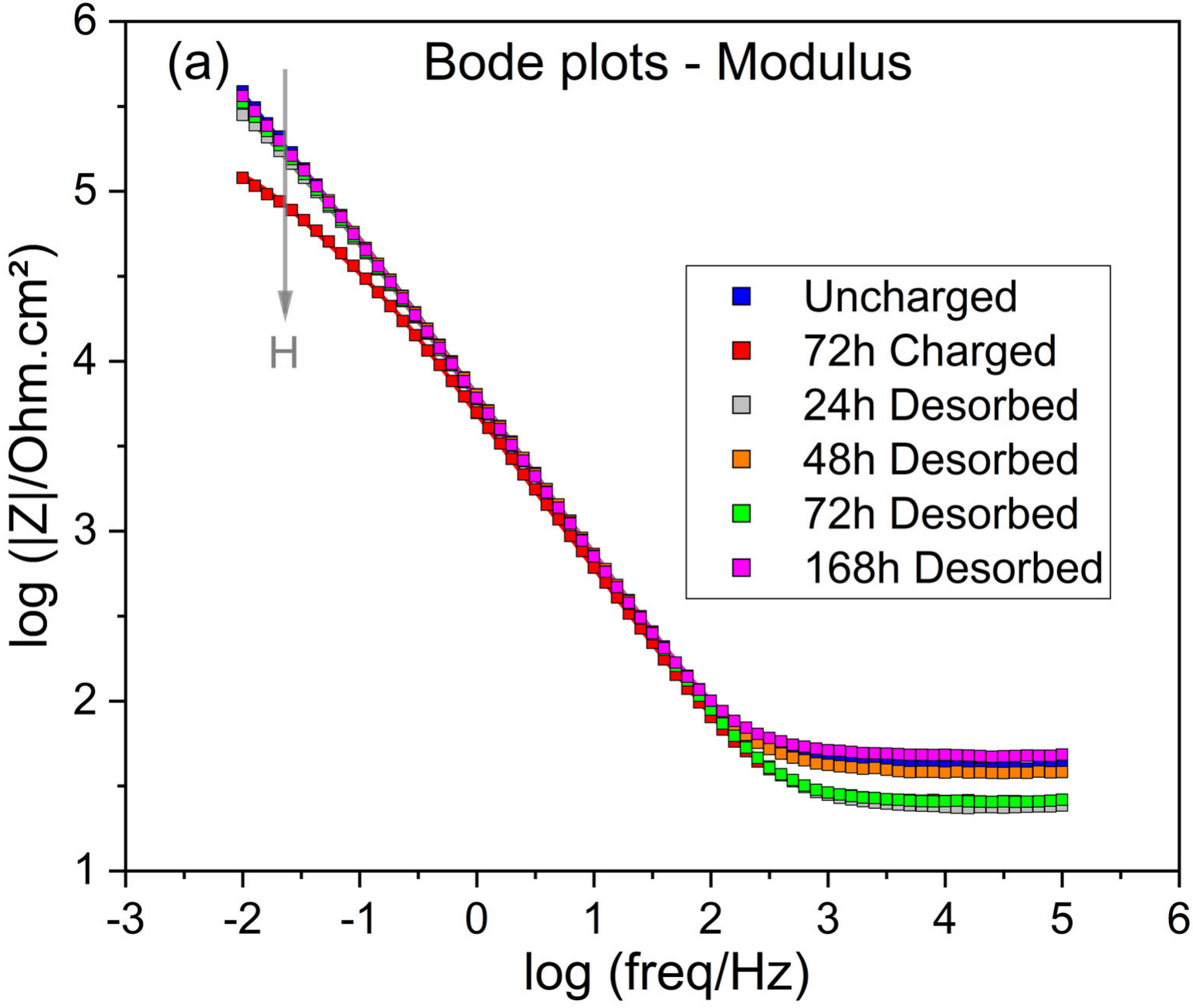
(a)
Bode plots - Modulus
H
Uncharged
72h Charged
24h Desorbed
48h Desorbed
72h Desorbed
168h Desorbed
log (|Z|/Ohm.cm²)
log (freq/Hz)
6
5
4
3
2
1
-3
-2
-1
0
1
2
3
4
5
6

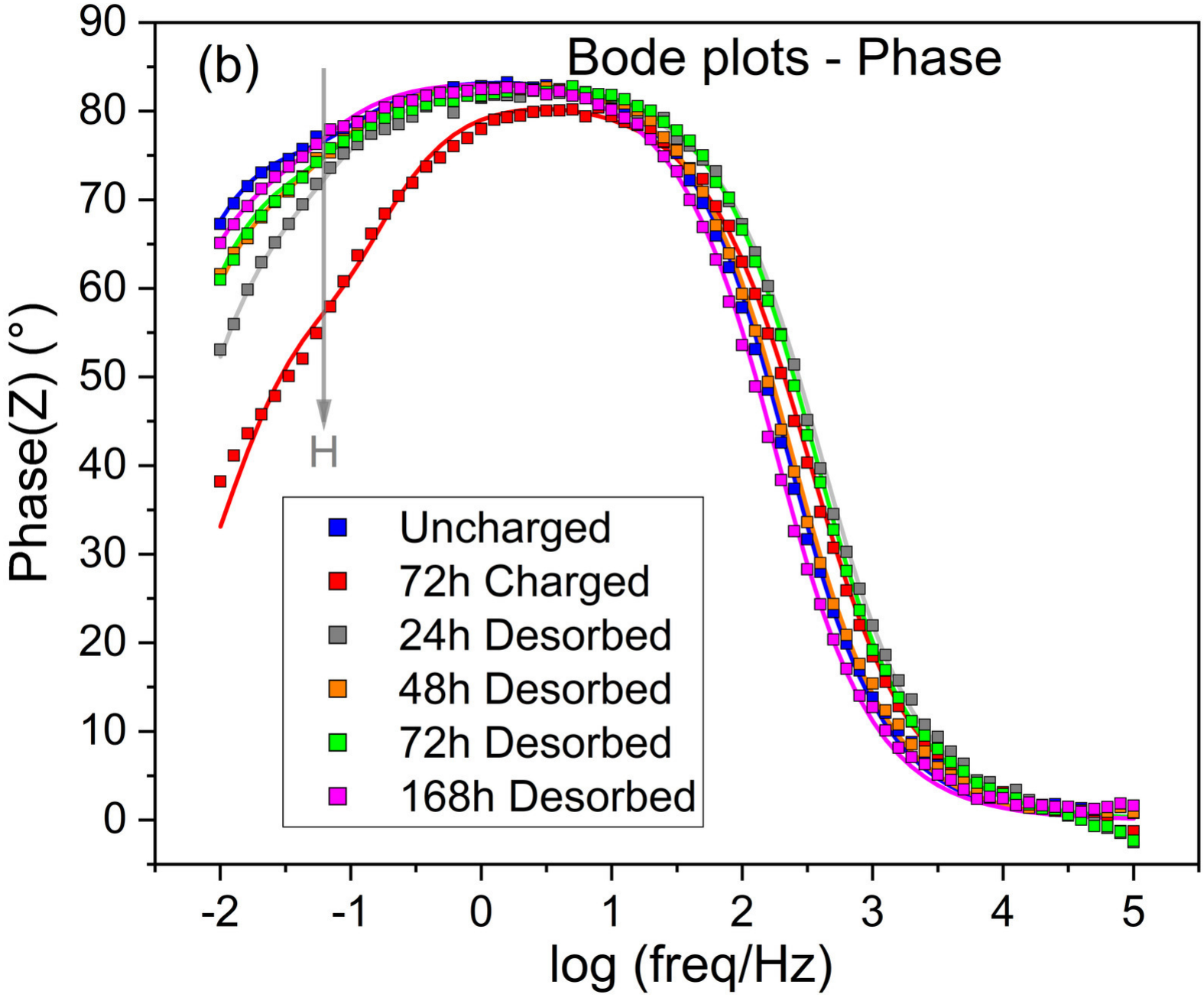
(b)
Bode plots - Phase
Phase(Z) (°)
log (freq/Hz)
H
Uncharged
72h Charged
24h Desorbed
48h Desorbed
72h Desorbed
168h Desorbed
90
80
70
60
50
40
30
20
10
0
-2
-1
0
1
2
3
4
5

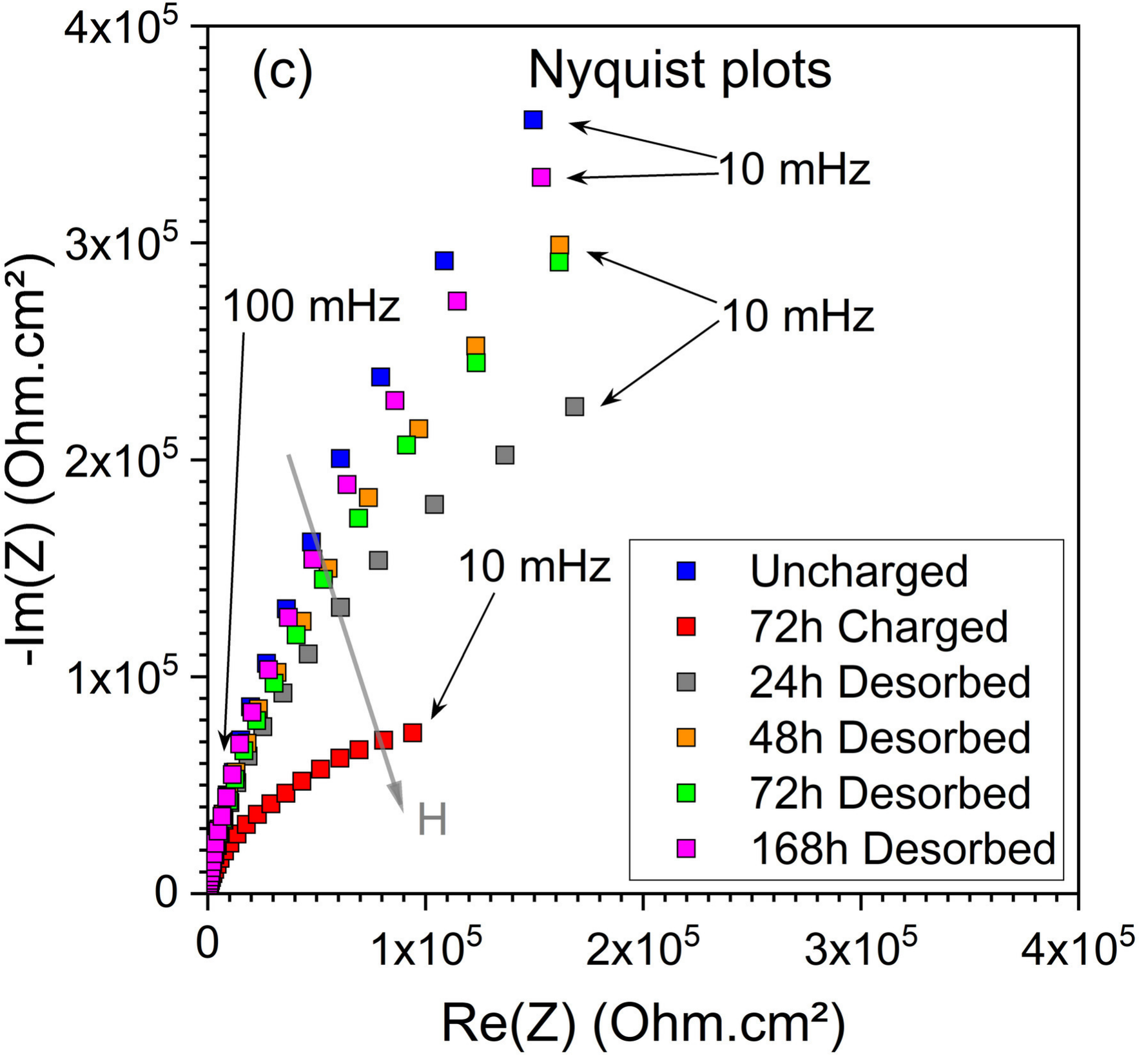
(c)
Nyquist plots
10 mHz
10 mHz
100 mHz
10 mHz
H
Uncharged
72h Charged
24h Desorbed
48h Desorbed
72h Desorbed
168h Desorbed
-Im(Z) (Ohm.cm²)
Re(Z) (Ohm.cm²)
0
1x10⁵
2x10⁵
3x10⁵
4x10⁵

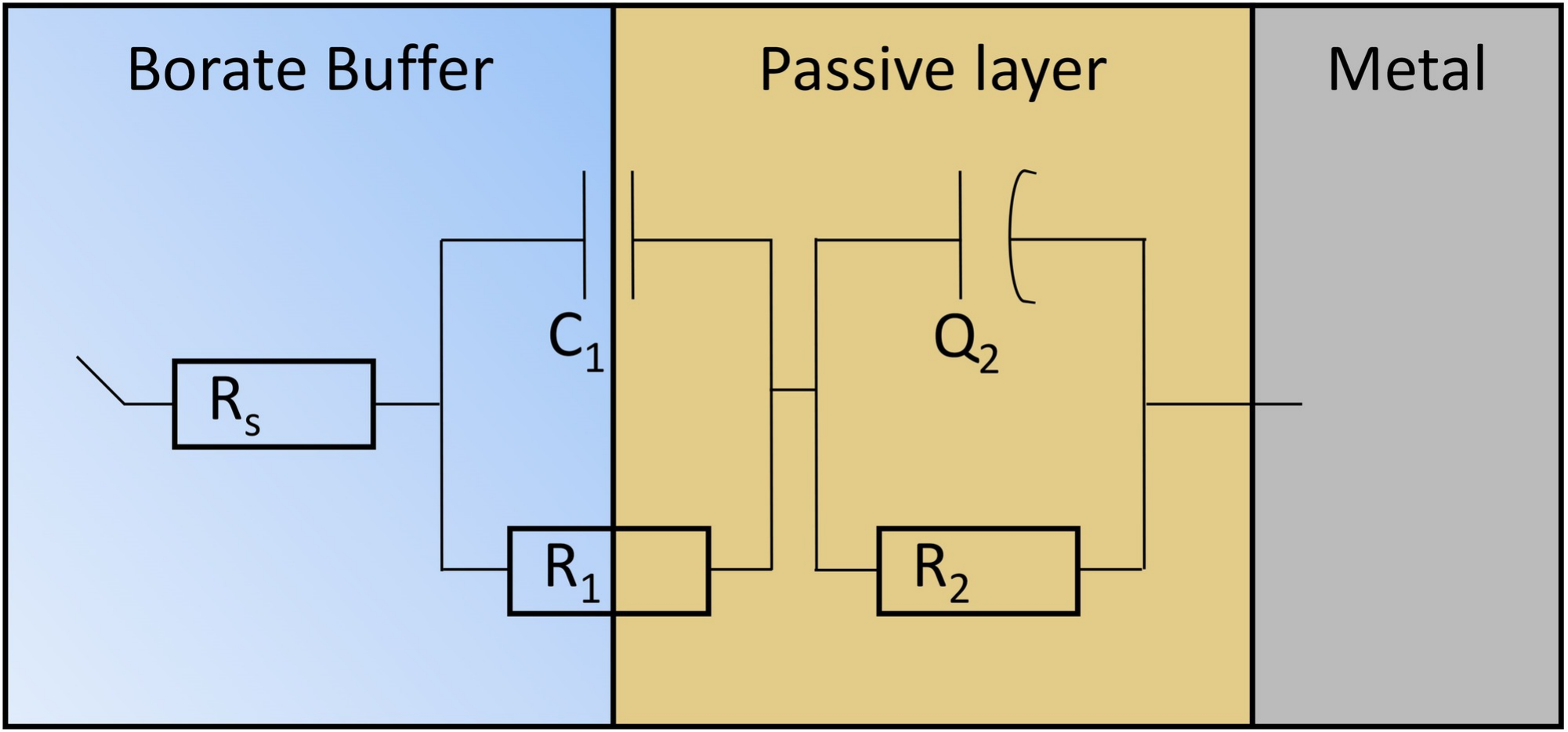
Borate Buffer
Passive layer
Metal
C_1
Q_2
R_s
R_1
R_2

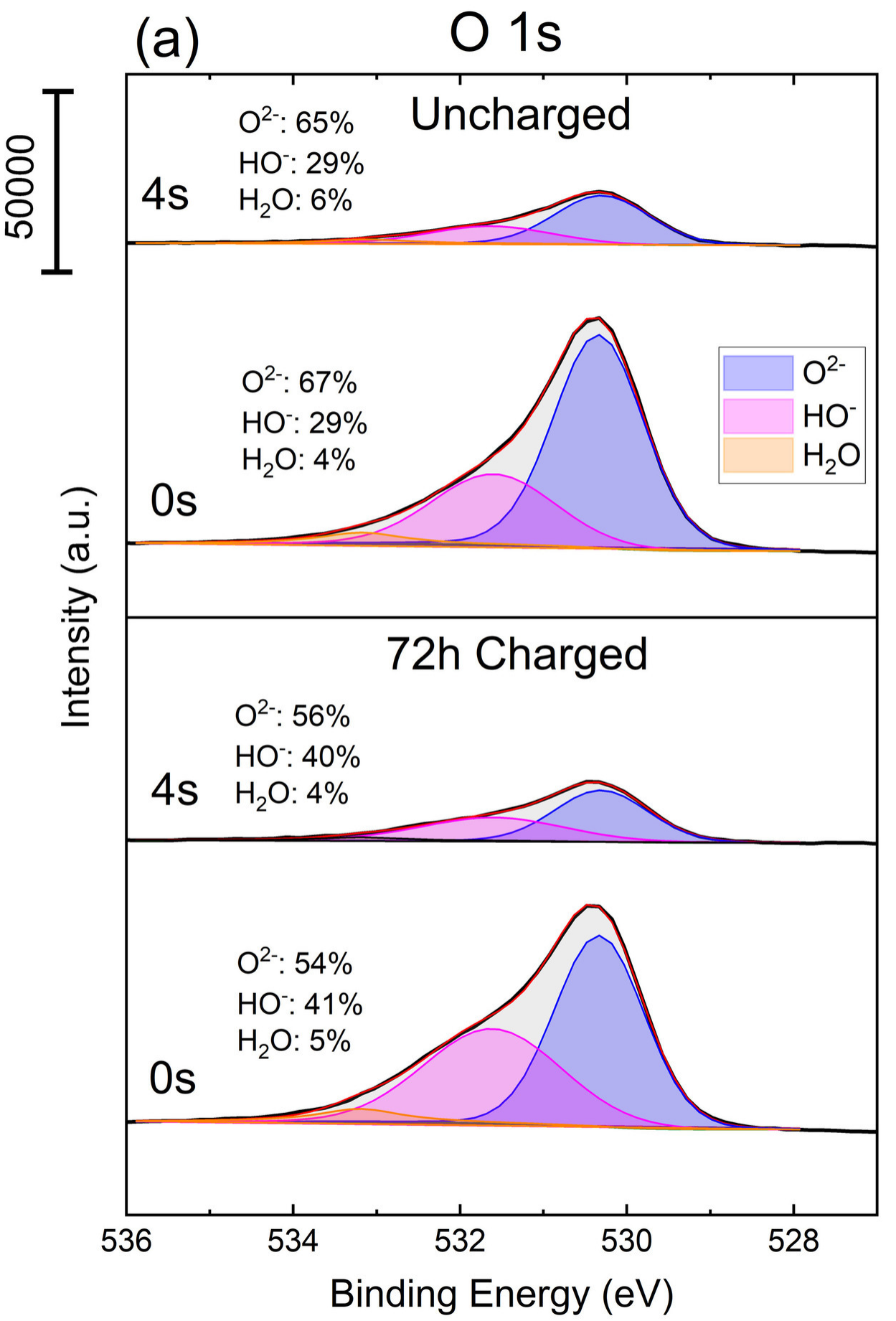
(a)
O 1s
50000
Uncharged
O^{2-}: 65%
HO^-: 29%
H_2O: 6%
4s
O^{2-}: 67%
HO^-: 29%
H_2O: 4%
0s
O^{2-}
HO^-
H_2O
72h Charged
O^{2-}: 56%
HO^-: 40%
H_2O: 4%
4s
O^{2-}: 54%
HO^-: 41%
H_2O: 5%
0s
Intensity (a.u.)
536
534
532
530
528
Binding Energy (eV)

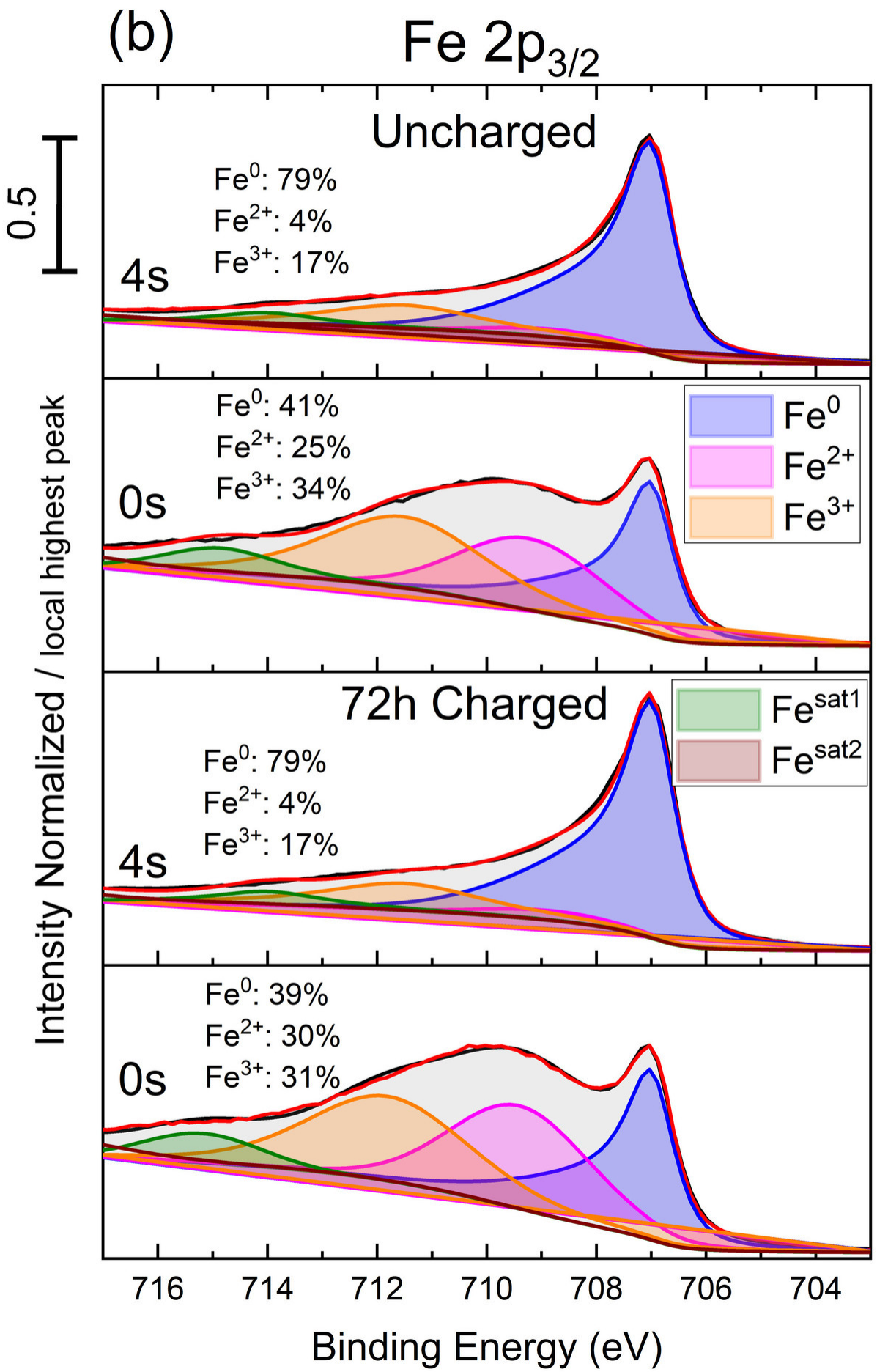
(b)
Fe 2p3/2
Uncharged
Fe0: 79%
Fe2+: 4%
Fe3+: 17%
4s
0.5
Fe0: 41%
Fe2+: 25%
Fe3+: 34%
0s
Fe0
Fe2+
Fe3+
72h Charged
Fe0: 79%
Fe2+: 4%
Fe3+: 17%
4s
Fesat1
Fesat2
Fe0: 39%
Fe2+: 30%
Fe3+: 31%
0s
Intensity Normalized / local highest peak
716
714
712
710
708
706
704
Binding Energy (eV)

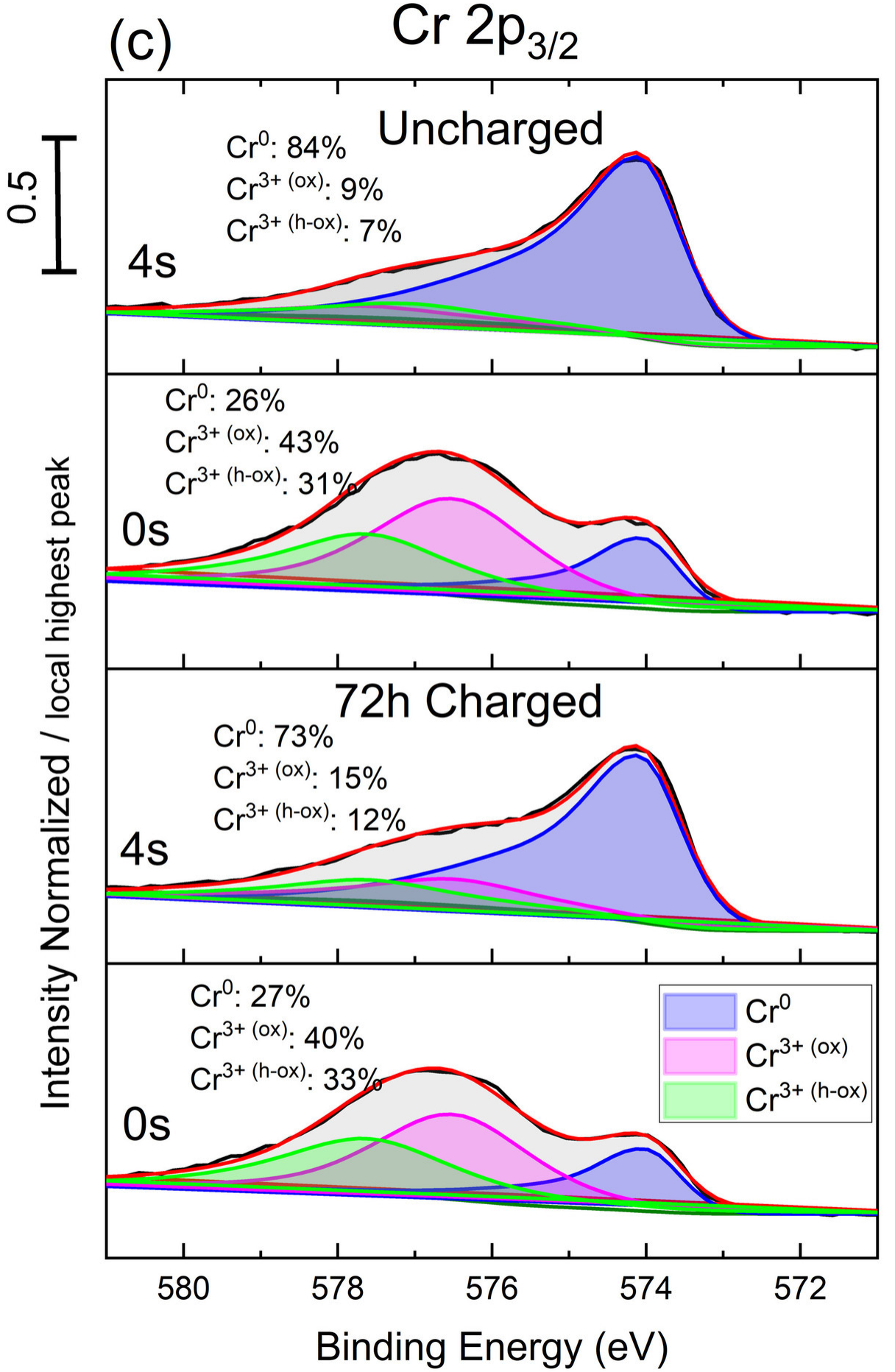
(c)
Cr 2p3/2
Uncharged
Cr0: 84%
Cr3+ (ox): 9%
Cr3+ (h-ox): 7%
4s
0.5
Cr0: 26%
Cr3+ (ox): 43%
Cr3+ (h-ox): 31%
0s
72h Charged
Cr0: 73%
Cr3+ (ox): 15%
Cr3+ (h-ox): 12%
4s
Cr0: 27%
Cr3+ (ox): 40%
Cr3+ (h-ox): 33%
0s
Cr0
Cr3+ (ox)
Cr3+ (h-ox)
Intensity Normalized / local highest peak
580
578
576
574
572
Binding Energy (eV)

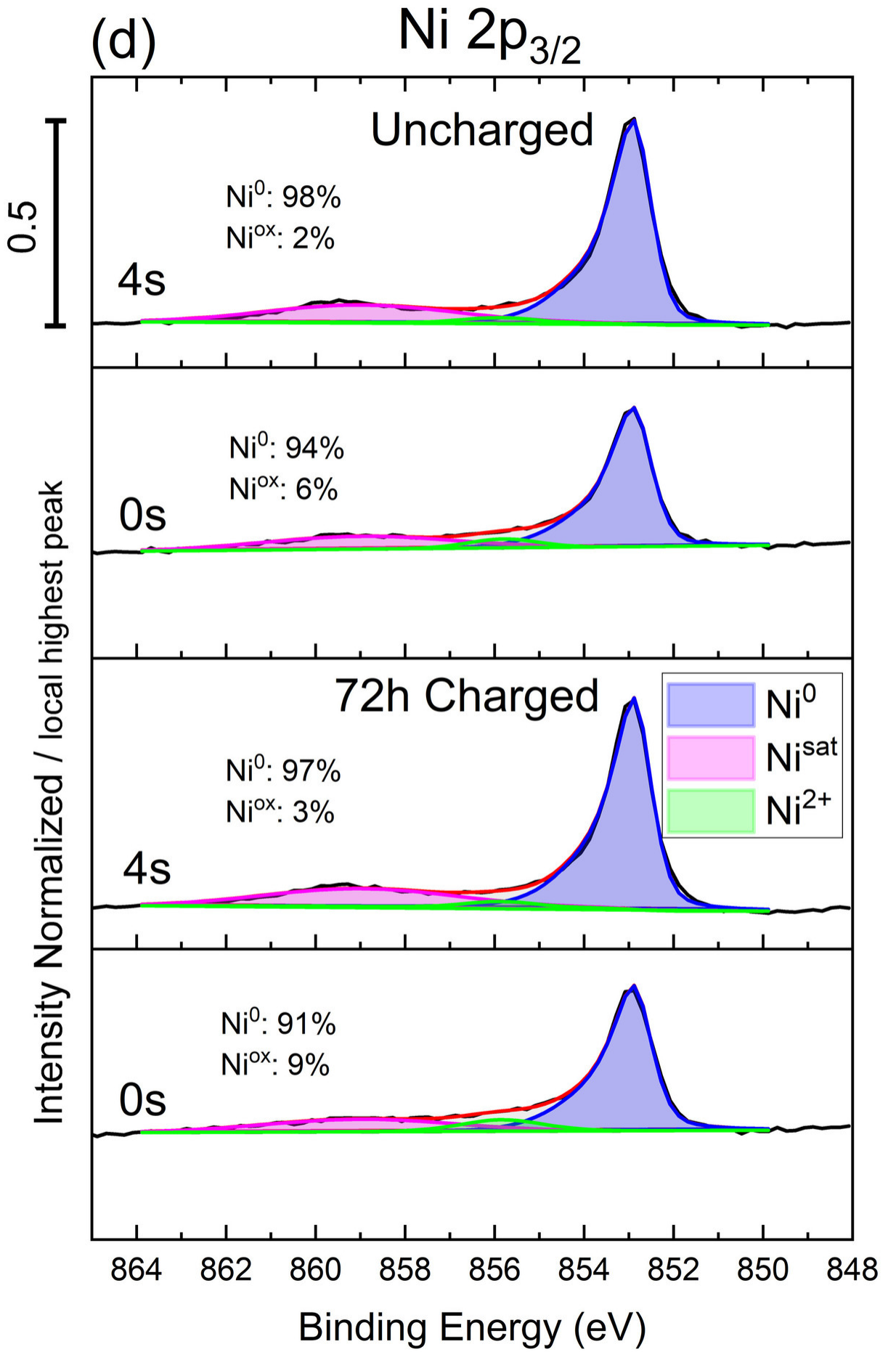
(d)
Ni 2p3/2
Uncharged
Ni0: 98%
Niox: 2%
4s
0.5
Ni0: 94%
Niox: 6%
0s
72h Charged
Ni0: 97%
Niox: 3%
4s
Ni0
Nisat
Ni2+
Ni0: 91%
Niox: 9%
0s
Intensity Normalized / local highest peak
864
862
860
858
856
854
852
850
848
Binding Energy (eV)

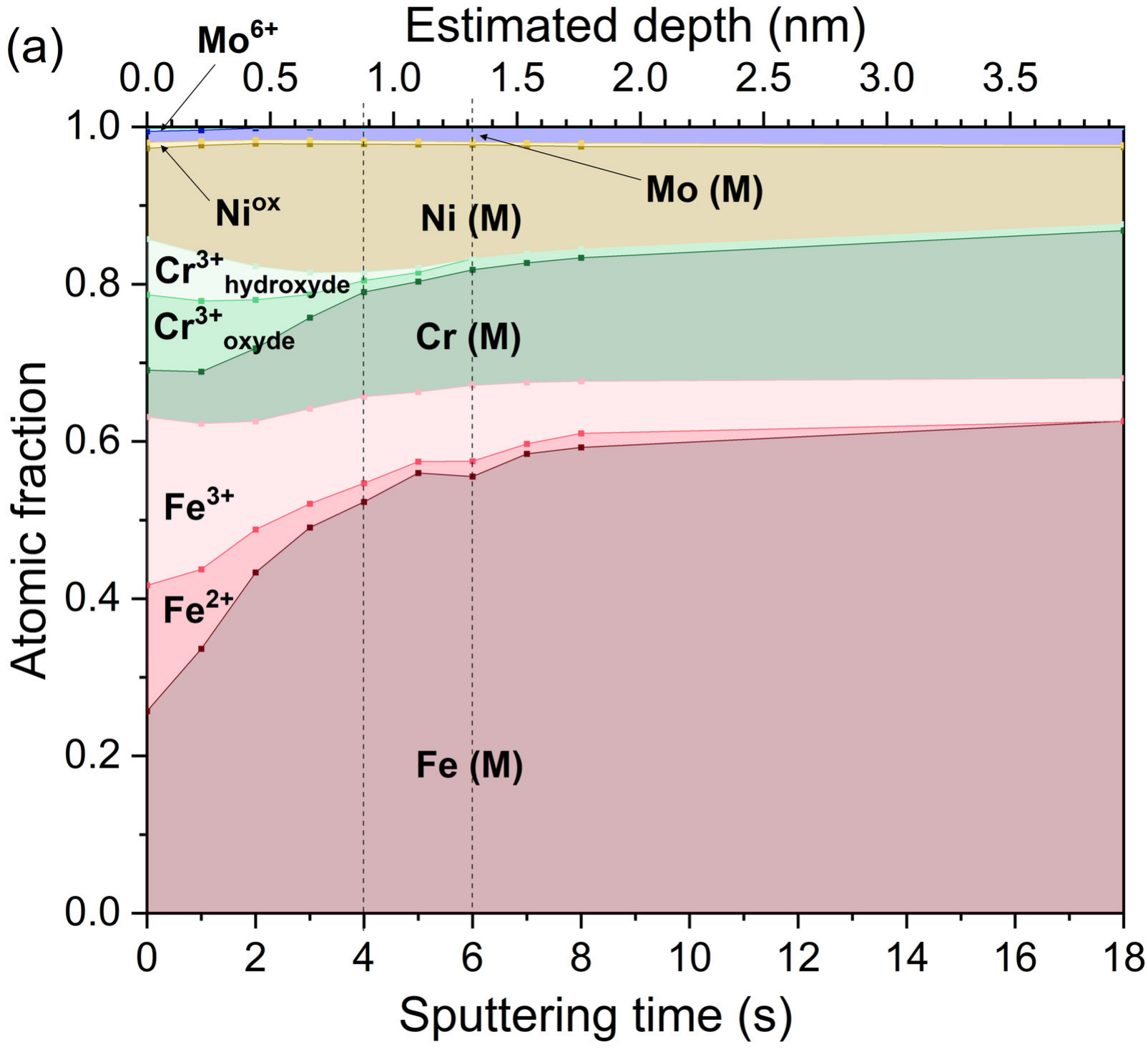
(a)
Mo6+
Estimated depth (nm)
0.0
0.5
1.0
1.5
2.0
2.5
3.0
3.5
Niox
Ni (M)
Mo (M)
Cr3+ hydroxyde
Cr3+ oxyde
Cr (M)
Fe3+
Fe2+
Fe (M)
Atomic fraction
0.0
0.2
0.4
0.6
0.8
1.0
0
2
4
6
8
10
12
14
16
18
Sputtering time (s)

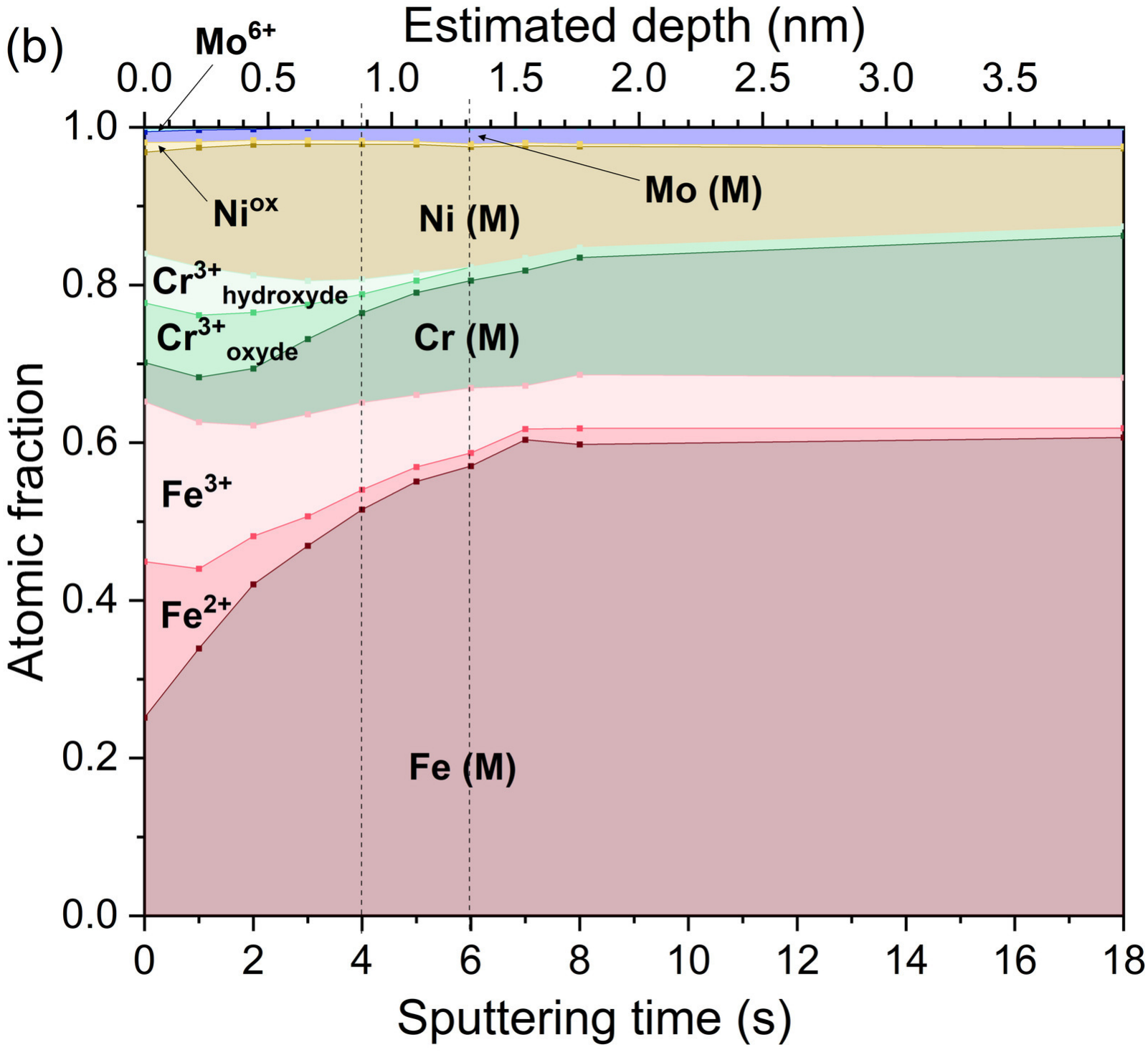
(b)
Mo6+
Estimated depth (nm)
0.0
0.5
1.0
1.5
2.0
2.5
3.0
3.5
Niox
Ni (M)
Mo (M)
Cr3+ hydroxyde
Cr3+ oxyde
Cr (M)
Fe3+
Fe2+
Fe (M)
Atomic fraction
0.0
0.2
0.4
0.6
0.8
1.0
0
2
4
6
8
10
12
14
16
18
Sputtering time (s)

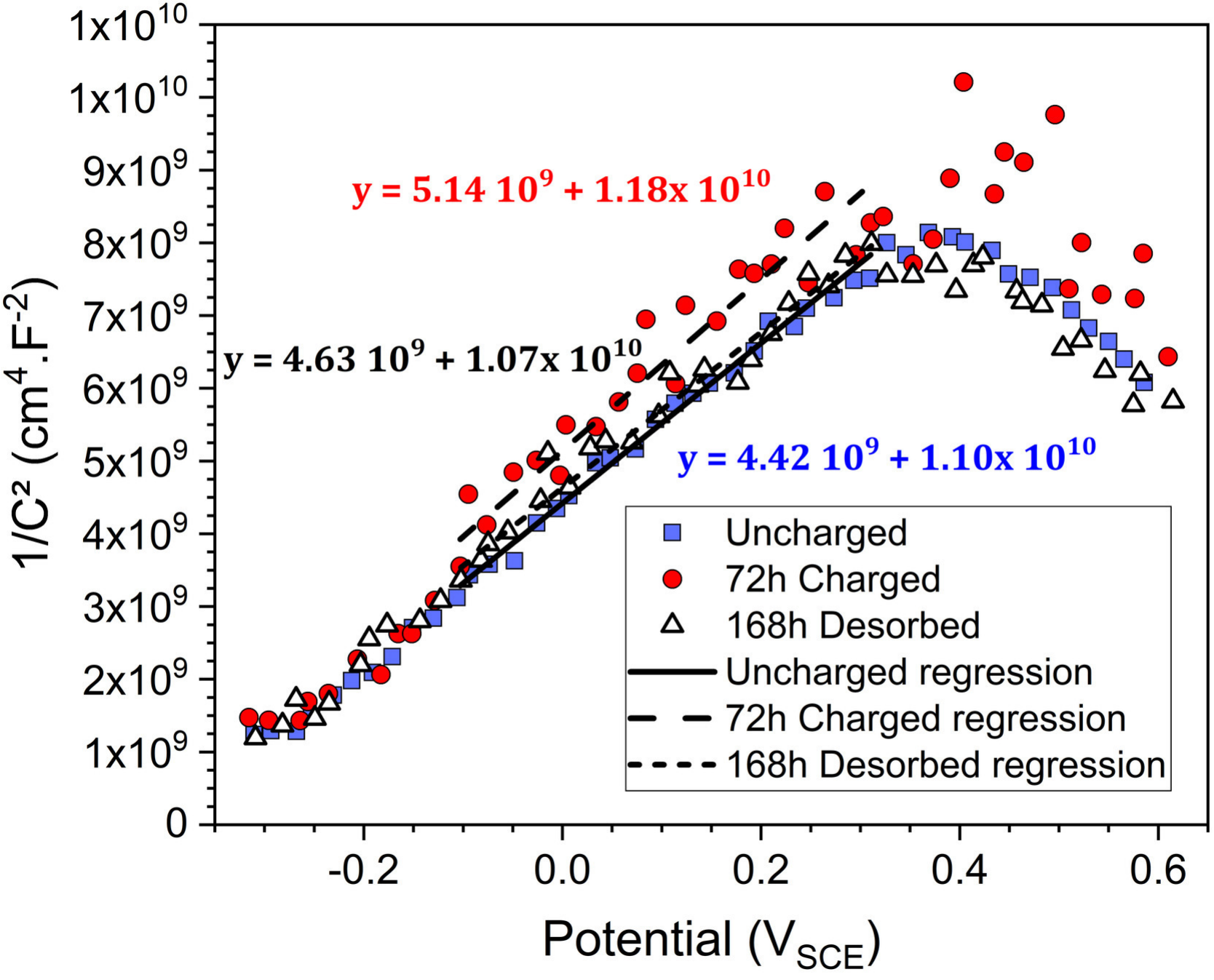
1x10^10
1x10^10
9x10^9
8x10^9
7x10^9
6x10^9
5x10^9
4x10^9
3x10^9
2x10^9
1x10^9
0
1/C² (cm⁴.F⁻²)
y = 5.14 10^9 + 1.18x 10^10
y = 4.63 10^9 + 1.07x 10^10
y = 4.42 10^9 + 1.10x 10^10
Uncharged
72h Charged
168h Desorbed
Uncharged regression
72h Charged regression
168h Desorbed regression
-0.2
0.0
0.2
0.4
0.6
Potential (V_SCE)

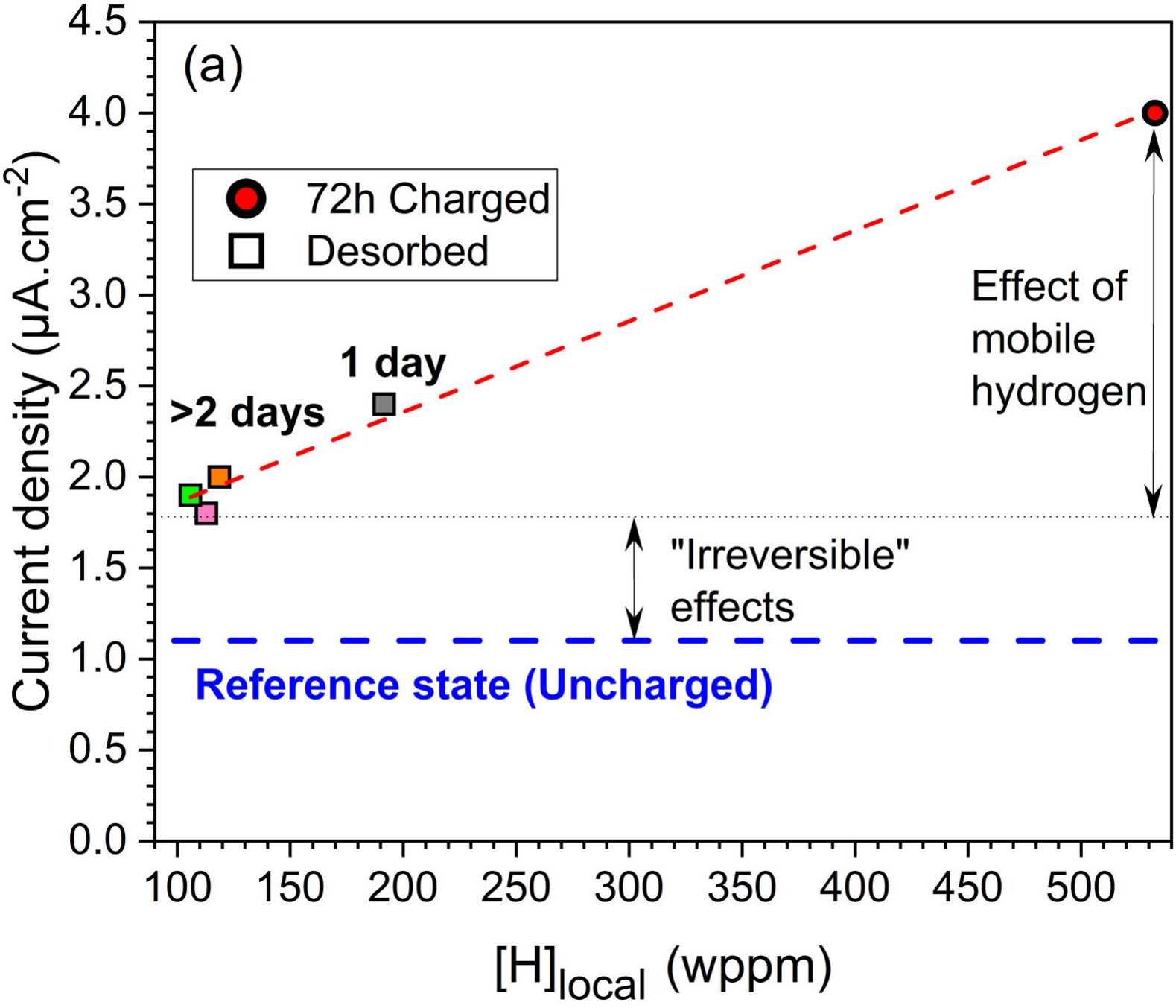
(a)
72h Charged
Desorbed
1 day
>2 days
Effect of mobile hydrogen
"Irreversible" effects
Reference state (Uncharged)
Current density (μA.cm-2)
[H]local (wppm)
4.5
4.0
3.5
3.0
2.5
2.0
1.5
1.0
0.5
0.0
100
150
200
250
300
350
400
450
500

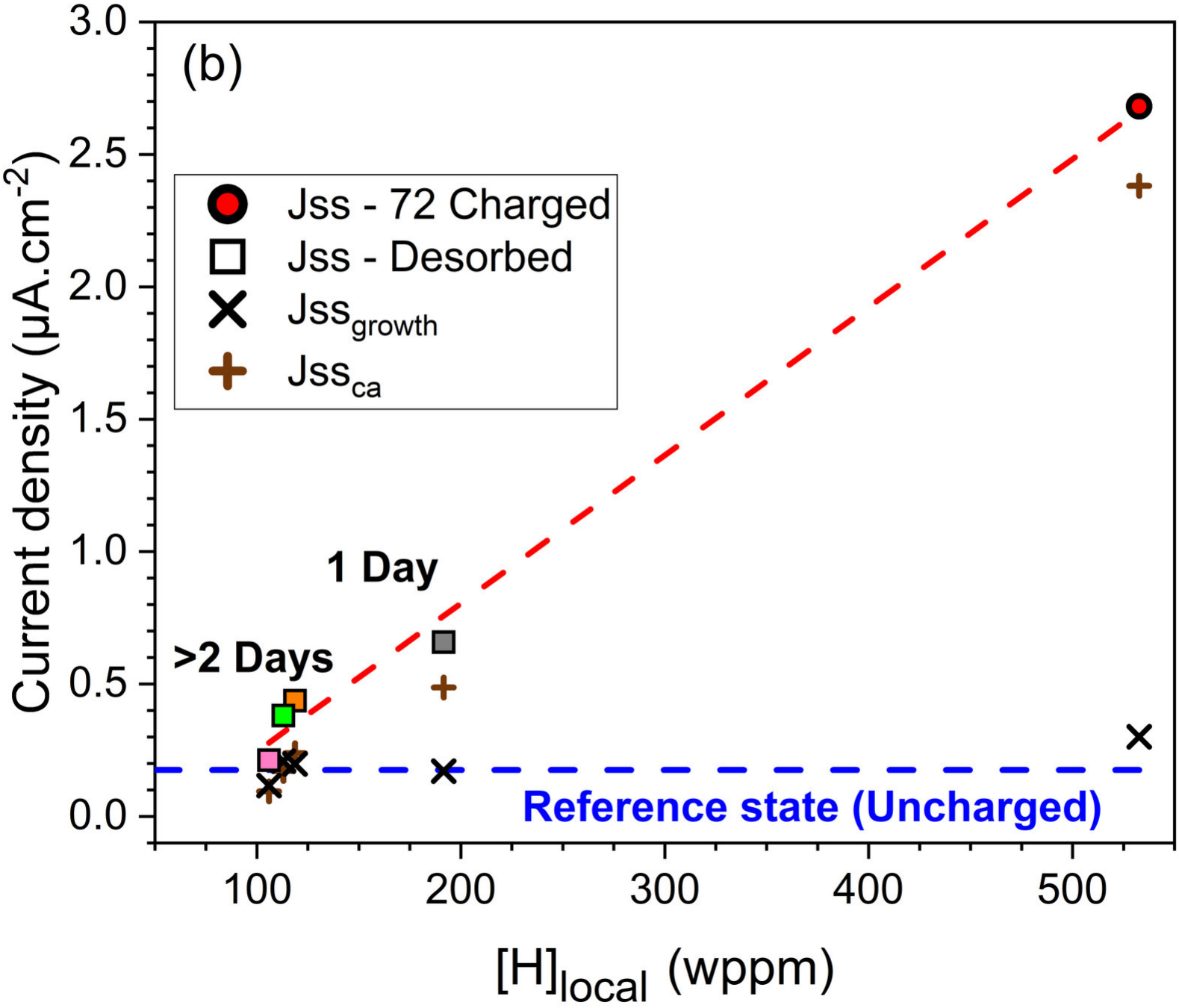
(b)
Jss - 72 Charged
Jss - Desorbed
Jss$_{growth}$
Jss$_{ca}$
1 Day
>2 Days
Reference state (Uncharged)
Current density (μA.cm^{-2})
[H]$_{local}$ (wppm)
3.0
2.5
2.0
1.5
1.0
0.5
0.0
100
200
300
400
500

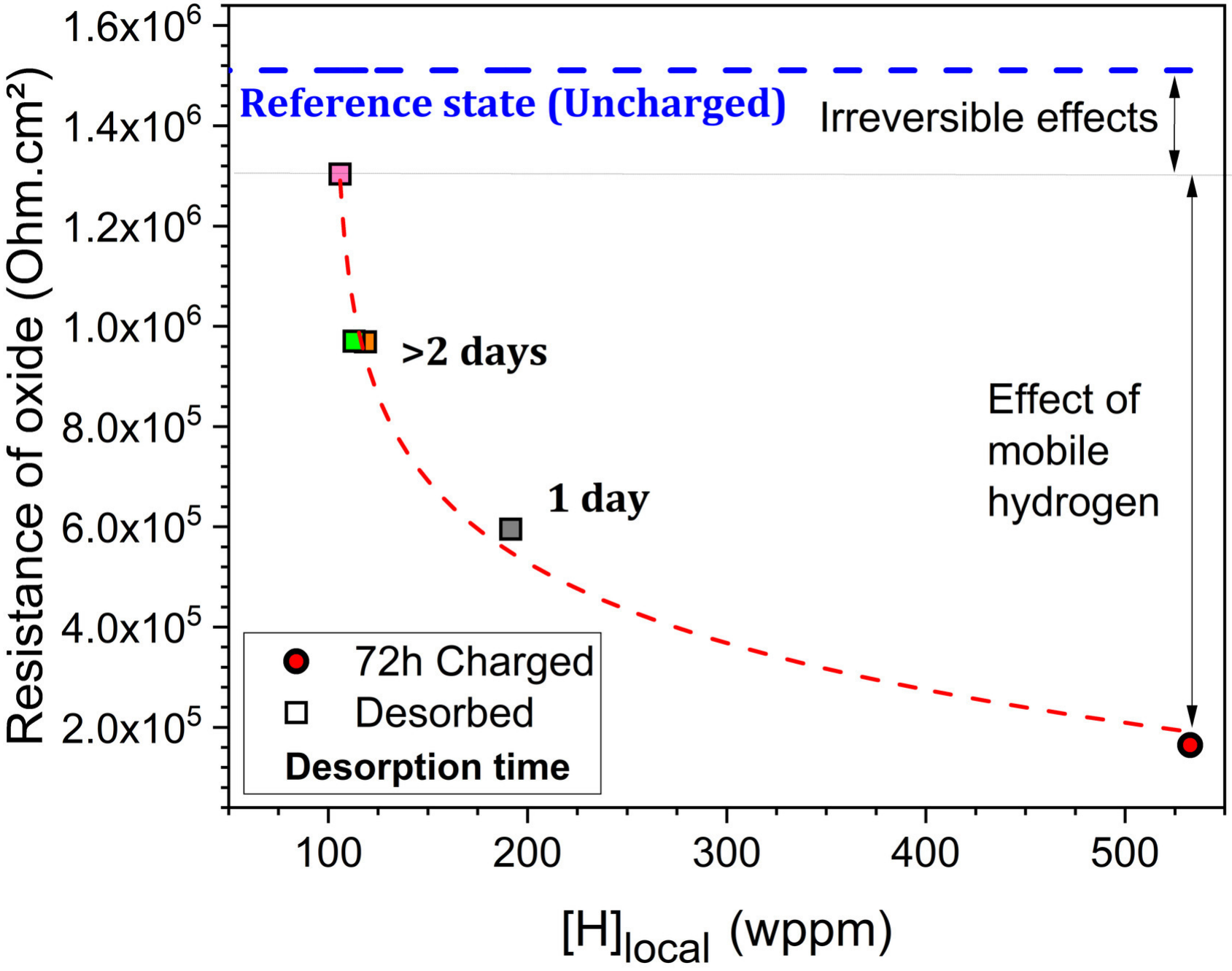
Reference state (Uncharged)
Irreversible effects
>2 days
1 day
Effect of mobile hydrogen
72h Charged
Desorbed
Desorption time
Resistance of oxide (Ohm.cm²)
1.6x10⁶
1.4x10⁶
1.2x10⁶
1.0x10⁶
8.0x10⁵
6.0x10⁵
4.0x10⁵
2.0x10⁵
100
200
300
400
500
[H]local (wppm)

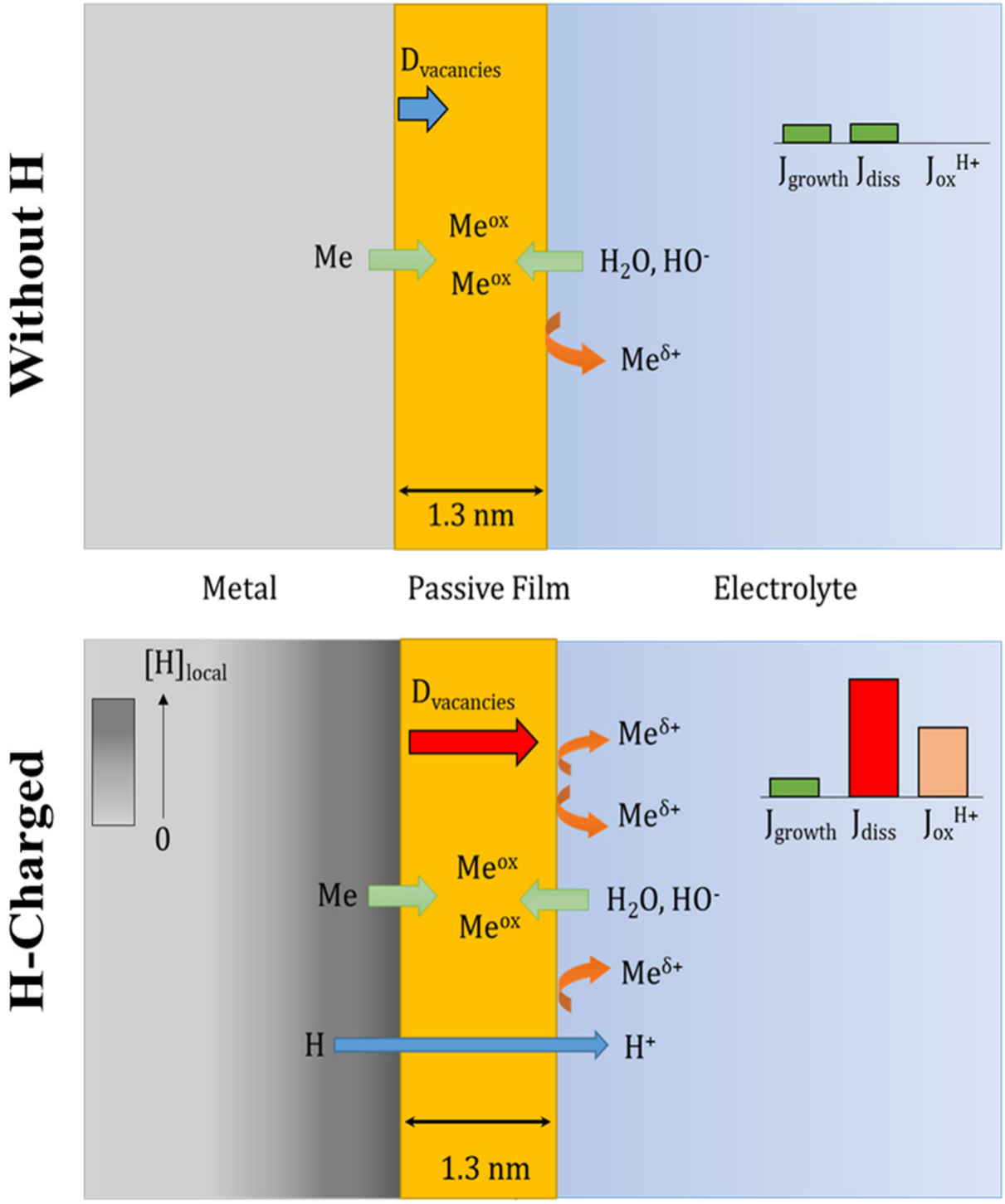
Without H
$D_{vacancies}$
Me
Me^{ox}
Me^{ox}
H_2O, HO^-
$Me^{\delta+}$
1.3 nm
J_{growth} J_{diss} J_{ox}^{H+}
Metal
Passive Film
Electrolyte
H-Charged
$[H]_{local}$
0
$D_{vacancies}$
$Me^{\delta+}$
$Me^{\delta+}$
Me
Me^{ox}
Me^{ox}
H_2O, HO^-
$Me^{\delta+}$
H
H^+
1.3 nm
J_{growth} J_{diss} J_{ox}^{H+}